Ru-RuO$_2$ nano-heterostructures stabilized by the sacrificing oxidation strategy of Mn$_3$O$_4$ substrate for boosting acidic oxygen evolution reaction

Xin Long [a], Bin Zhao [a,*], Qianqian Zhao [a], Xuexian Wu [a], Meng-Nan Zhu [b], Renfei Feng [c], Mohsen Shakouri [c], Yu Zhang [d], Xinxin Xiao [e], Jiujun Zhang [f], Xian-Zhu Fu [a], Jing-Li Luo [a,*]

[a] *Shenzhen Key Laboratory of Polymer Science and Technology, Guangdong Research Center for Interfacial Engineering of Functional Materials, College of Materials Science and Engineering, Shenzhen University, Shenzhen 518060, China*
[b] *Department of Chemical and Materials Engineering, University of Alberta, Edmonton, Alberta T6G 2G6, Canada*
[c] *Canadian Light Source Inc., Saskatoon, S7N 0X4, Saskatchewan, Canada*
[d] *Instrumental Analysis Center of Shenzhen University (Lihu Campus), Shenzhen University, Shenzhen, Guangdong 518055, China*
[e] *Department of Chemistry and Bioscience, Aalborg University, Fredrik Bajers Vej 7H, 9220 Aalborg East, Denmark*
[f] *Institute for Sustainable Energy, College of Sciences, Shanghai University, Shanghai 200444, China*

ARTICLE INFO

ABSTRACT

Designing anodic electrocatalysts with high activity and robust stability for acidic oxygen evolution reaction (OER) is significant for the large-scale promotion of sustainable proton exchange membrane water electrolysis (PEMWE). Most reported Ru-based electrocatalysts tend to further improve activity at the expense of stability. Herein, we report the synthesis of crystalline Mn$_3$O$_4$ supported Ru-RuO$_2$ nano-heterostructures as the anodic electrocatalyst that only requires a low overpotential of 182 mV (10 mA cm^{-2}) for acidic OER, accompanied with a record stability of 400 h in 0.5 M H$_2$SO$_4$. The results of XPS, ICP-MS, and XAS indicate that the Mn$_3$O$_4$ substrate plays a crucial role in stabilizing Ru-RuO$_2$ nano-heterostructure by preventing Ru from over-oxidation and dissolution. Meanwhile, DEMS with isotope labeling reveals that the Ru-RuO$_2$ nano-heterostructure contributes to suppressing lattice oxygen oxidation mechanism (LOM) and concurrently expediting the involvement of adsorbate evolution mechanism (AEM) for boosting the acidic OER performance.

1. Introduction

Electrochemical water splitting is broadly regarded as a promising and sustainable technique for producing green hydrogen, crucial to achieving the global mission of carbon neutrality [1]. Nowadays, the alkaline water electrolysis with a long research history has been equipped with a mature process route and is commercially available for producing hydrogen, but it still suffers from some fundamentally practical limitations, such as high ohmic resistance, low operational pressure, and the crossover of gases [2]. In contrast, employing a polymer-based proton exchange membrane under acidic medium, the well-known PEMWE has garnered extensive attention because it can effectively solve the above problems of its alkaline counterpart with markedly enhanced performance. Nevertheless, the large-scale deployment of PEMWE is greatly hampered by the lack of acidic OER electrocatalysts with high activity, robust stability, and low cost [2,3]. To date, RuO$_2$ is considered as the benchmark electrocatalyst for acidic

OER but its inferior dissolution resistance makes it difficult to put into PEMWE commercial operation [4]. Although IrO$_2$ is more stable than RuO$_2$ in acidic media, the price of Ir is about 7.5 times higher than Ru [3]. Hence, IrO$_2$ is costly to serve as commercial anode electrocatalysts for PEMWE. Therefore, the elaborate design of Ru-based electrocatalysts to further enhance acidic OER performance and durability is highly imperative.

The thorough understanding of acidic OER reaction mechanism can provide insightful guidance for the design of rational electrocatalysts. There are two major mechanisms for acidic OER process of Ru-based electrocatalysts: the adsorbate evolution mechanism (AEM) and the lattice oxygen oxidation mechanism (LOM). The former generates routine OER intermediates (OH*, O*, and OOH*) from the adsorbates (H$_2$O, in acidic medium) and exhibits a universal volcano relationship between catalytic activity and binding energy thermodynamically [5–7]; while the latter involves direct O-O coupling between the oxo-intermediates and lattice oxygen which is in favor of the OER

kinetics process [8,9]. It has been proposed that the low intrinsic activity and poor stability of rutile RuO_2 stems from the participation of lattice oxygen, leading to the collapse of catalytic structure and undermining the stability of Ru-based electrocatalysts in acid [10–12]. To accomplish stability in Ru-based electrocatalysts, it is necessary to accelerate the AEM pathway while inhibiting the involvement of the LOM pathway, which demands the design of Ru-based electrocatalysts with optimal surface energies for intermediates [13]. Moreover, excessive oxidation of Ru atoms at high overpotentials leads to high valence state $Ru^{\delta>4+}$ species which are beneficial for high acidic OER activity but are soluble. In consequence, the high activity of RuO_2 only remains few hours and then the Ru ions rapidly dissolve into the electrolyte [11,14–16].

Recently, enormous efforts have been undertaken to develop advanced Ru-based electrocatalysts via various strategies including engineering heterostructures (Ru-RuO$_2$@NPC) [17], doping (Co-RuO$_2$) [18], strain effect (Ru$_1$-Pt$_3$Cu) [12], ultra-thin two-dimensional nanostructure (ultra-thin RuO_2 nanosheets) [19], solid-solution oxides ($Mn_{0.75}Ru_{0.25}O_{2-d}$) [20], and so on. Nevertheless, the stability of most Ru-based electrocatalysts reported so far is still unsatisfactory, not reaching industrial application requirements [21]. It is desirable to develop new strategies to achieve simultaneously both enhanced stability and activity for electrocatalysts. Recent literature revealed that constructing a RuO_2/CoO_x hybrid electrocatalyst could form a stable interface to prevent the excessive oxidation of RuO_2 and break the stability-activity seesaw relation on Ru-based electrocatalysts [22]. Experimental and theoretical calculations verify that the sacrificing oxidation is an avail strategy to simultaneously improve activity and stability. Meanwhile, the catalyst-support interaction also makes contributions to improving acidic OER performance, rational interfacial engineering plays a crucial role in creating new active sites and stabilizing components [22–24]. In previous work, an inspiring approach in the use of Mn_3O_4 as the substrate was described by Kim et. al, who studied metal-oxide-supported catalytic systems and discovered the spontaneous deposition of Pt on the surface of Mn_3O_4 particles. This composite system presented better ORR performance than Pt/C [25]. Moreover, Gowda et. al provided a detailed discussion of Mn_3O_4 as the possible electrocatalyst substitute for energy conversion, and proposed that increased oxidation sites are advantageous to electrocatalytic property [26]. Hence, utilizing earth-abundant and economical metallic oxide Mn_3O_4 as substrate components can reduce the use of precious metal Ru and benefit sustainable development. It is expected that the construction of a sacrificial substrate could effectively balance the catalytic activity and stability of high-valence $Ru^{\delta>4}$ species. Combining the sacrificing oxidation of substrate and heterostructure synergistic effect could be an effective strategy to simultaneously enhance both stability and activity in acidic OER, but such work is still challenging and rarely reported.

Herein, inspired by the above strategy, we report the crystalline Mn_3O_4 supported Ru-RuO_2 nano-heterostructures on carbon paper as a highly active and stable electrocatalyst under acidic condition. Ru-RuO_2/Mn_3O_4/CP exhibits a significantly high activity (only 182 mV at 10 mA cm^{-2} and 1324.6 A g_{Ru}^{-1} of mass activity at 1.50 V vs. RHE) and maintains outstanding long-term stability (400 h) under continuous operation in 0.5 M H_2SO_4. Besides, the anodic electrocatalyst Ru-RuO_2/ Mn_3O_4/CP coupled with a commercial Pt/C (20 wt%) displays continuous water electrolysis for more than 65 h at 50 mA cm^{-2} in the practical PEM electrolyzer. X-ray photoelectron spectroscopy, time-dependent elemental analysis, and X-ray absorption spectroscopy results reveal that the enhanced activity and stability of Ru-RuO_2/Mn_3O_4/CP can be ascribed to the sacrificing oxidation of Mn_3O_4 substrate, which is efficient to prevent the electrocatalyst from the over-oxidation and dissolution of Ru species for acidic OER. *Operando* differential electrochemical mass spectrometry (DEMS) with isotope labeling measurements confirms the formation of Ru-RuO_2 nano-heterostructures can suppress the LOM pathway during OER, leading to promoted OER stability and activity in acidic media.

2. Experimental

2.1. Materials and synthesis

Ruthenium (III) chloride hydrate (RuCl$_3$·H$_2$O, 98%), ruthenium on carbon (Ru 5%, MW=101.07), tuthenium (IV) oxide (99.9%), poly-vinylpyrrolidone (PVP10, MW=58000) were obtained from Macklin. Manganese (II) chloride tetrahydrate (MnCl$_2$.4 H$_2$O, ≥99%), Nafion solution (~5% in a mixture of lower aliphatic alcohols and water) were obtained from Sigma-Aldrich. Water-^{18}O (H$_2$^{18}O, 97 at% ^{18}O) were purchased from Energy Chemical. All reagents were used as received without further purification.

The Ru-RuO_2/Mn_3O_4/CP electrocatalyst was synthesized following the previously reported impregnation method with minor modifications [27]. Before deposition, commercial carbon paper (CP) was cut into pieces of 1 × 1.5 cm^{-2} and respectively treated with acetone, hydro-chloric acid (1 M) and deionized water for 30 min under ultra-sonication to remove surface oily impurity and oxides. In a typical procedure, RuCl$_3$·H$_2$O (0.7 mmol), MnCl$_2$.4 H$_2$O (0.7 mmol) and 160 mg PVP were dissolved into 5 mL deionized water (18.2 MΩ) and then stirred overnight before loading. The impregnation method was applied to directly synthesize electrode with catalysts in situ growing on the CP substrate. Specifically, the CP was impregnated into the precursor solution for 5 min and then dried in a vacuum oven at 60 °C. After drying for 20 min, the precursor modified CP was transferred into a muffle furnace and heated to 400 °C at 10 °C min^{-1} in air atmosphere, and then held for 6 h. Furthermore, the pristine Ru-RuO_2/CP (without Mn precursor) and Mn_3O_4/CP (without Ru precursor) were obtained separately with the same experimental procedure. The Ru-RuO_2/Mn_3O_4, Ru-RuO_2, and Mn_3O_4 electrocatalysts grown on carbon paper were directly used as the working electrode in a standard three-electrode system.

For the preparation of control group, 5 mg catalyst was dispersed in 950 μL mixture of water and ethanol (1:8.5, v/v), and then 50 μL of 5 wt % Nafion solution was added. The mixed solution was followed by ultrasonication for 30 min to obtain a homogeneous catalyst suspension. Afterwards, 100 μL catalyst ink was dropped on the carbon paper (loading area 1 × 1 cm^{-2}) yielding a mass loading of 0.5 mg cm^{-2}. The modified electrode (commercial RuO$_2$/CP and RuC/CP) was dried at ambient temperature before electrochemical measurements.

2.2. Catalyst characterization

The as-synthesized electrocatalysts were characterized by field-emission SEM images using Hitachi SU-70 system (probe current 100 nA, accelerating voltages 10 kV), which was equipped with Oxford INCA (Aztec) X-ray spectroscopy (EDS) detector at 20 kV to analyze composition. TEM, HRTEM and HAADF-STEM images were performed on JEOL JEM-F200 system (acceleration voltage 200 kV) equipped with a EDS detector at 20 kV.

To study the phase composition of the sediment on the carbon paper, the vacuum dried powder was taken for X-ray diffraction (XRD) test. XRD spectra were recorded with a RIGAKU Smartlab using Cu Kα radiation (λ = 1.5406 Å). X-ray photoelectron spectroscopy (XPS) measurements were carried out on a Thermo Scientific ESCALAB 250Xi spectrometer. The K-edge X-ray absorption fine structure (XAFS) of Ru and Mn elements for electrocatalysts were recorded by synchrotron radiation light source using a hard X-ray beam of "VESPERS" at Canadian Light Source (CLS), Canada. The loading of Ru and Mn on carbon paper and the dissolution of catalysts during OER process were quantified by ICP-MS (Agilent ICP-MS 7700).

2.3. Electrocatalytic methods and Fabrication of membrane electrode assembly

All the electrochemical measurements including linear sweep voltammetry (LSV), electrochemical impedance spectroscopy (EIS),

electrochemical double-layer capacitance (C_{dl}), and Faradaic efficiency (FE) for acidic OER were conducted on a CHI 760E electrochemical workstation (CH Instruments, Inc., Shanghai, China) at room temperature with a standard three-electrode system. These electrocatalytic methods and membrane electrode assembly (MEA) test were described in Supplementary data in detail.

2.4. Differential electrochemical mass spectroscopy (DEMS) measurements

DEMS measurements were carried out using a QAS 100 device (Linglu Instruments, Shanghai). A saturated Ag/AgCl electrode and a Pt wire were used as the reference electrode and counter electrode, respectively. The working electrodes were prepared by sputtering Au onto 50 μm thick porus PTFE films. Then, the catalysts were dropped and casted onto the Au film with a mass loading of 0.75 mg cm^{-2}. All samples were labeled with ^{18}O isotopes by performing 10 CV cycles at a scan rate of 5 mV s^{-1} in 0.5 M H_2SO_4 using $H_2^{18}O$ as the solvent (All samples were scanned for LSV near the onset potential of OER). Afterward, the ^{18}O-labeled catalysts were rinsed with $H_2^{16}O$ for several times and dried to remove the residual $H_2^{18}O$ in order to avoid the interruption of surface adsorbed ^{18}O species to the observed $^{34}O_2$ ($^{16}O^{18}O$) MS signals. Finally, potential scans were carried out in a normal 0.5 M H_2SO_4 solution at appropriate potential windows and scan rate. In the meantime, the gaseous products including $^{32}O_2$ ($^{16}O^{16}O$), $^{34}O_2$ ($^{16}O^{18}O$), and $^{36}O_2$ ($^{18}O^{18}O$) during OER process were measured in real time by mass spectroscopy. Before the electrochemical measurements, all the electrolytes were purged with high-purity Ar to remove the dissolved oxygen.

2.5. Computational details

All the spin-polarized DFT calculations are conducted based on the Vienna Ab-inito Simulation Package (VASP) [28,29]. The electron-ion interactions are described by the Projected Augmented-Wave (PAW) potentials, while the exchange-correlation interactions are calculated by employing the Perdew-Burke-Enzerhof (PBE) functional of Generalized Gradient Approximation (GGA) with a Hubbard U extension (U value) of 3.9 eV, and 4.88 eV for Mn and Ru [30,31]. The vdW-D3 method developed by Grimme was employed to describe the van der Waals interaction [32]. The Ru-RuO$_2$ heterostructure is built using RuO$_2$ (101) and Ru (100). The plane-wave energy cutoff is set as 450 eV. The convergence threshold is set as 1.0×10^{-5} eV in energy and 0.05 eV per Angstrom in force. A vacuum layer of 15 Å is adopted to avoid the periodic interactions. The Brillouin zone is modeled by gamma centered Monkhorst-Pack scheme, in which the $4 \times 4 \times 1$ and $1 \times 3 \times 1$ grids are adopted for RuO$_2$ (110) and Ru-RuO$_2$, respectively.

The change in the Gibbs free energy of each reaction is calculated as follow:

$$\Delta G = \Delta E_{pot} + \Delta E_{ZPE} - T\Delta S$$

in which the ΔE_{pot}, ΔE_{ZPE} and the ΔS are referred to as the change in potential energy, the change in the zero-point energy, and the change in the entropy, respectively.

The zero-point energy was calculated by the summation of all vibrational frequencies.

$E_{ZPE} = \frac{1}{2}\sum h\nu$ where the ν corresponds to the vibrational frequency of each normal mode [33].

3. Results and discussion

3.1. Structural analysis

The electrocatalysts of Ru-RuO$_2$/Mn$_3$O$_4$/CP, Ru-RuO$_2$/CP, and Mn$_3$O$_4$/CP were synthesized in situ on carbon paper through an impregnation-calcination method based on a previous report, which was easily accessible for large-scale preparation [27]. The transmission electron microscopy (TEM) image in Fig. 1a obviously displays the anisotropic lattice fringes of the three phases in Ru-RuO$_2$/Mn$_3$O$_4$/CP, notably, the high-resolution Transmission Electron Microscope (HRTEM) image of Fig. 1b presents Ru (100) and RuO$_2$ (110) heterostructures loaded on Mn$_3$O$_4$ (105) exhibit plentiful defects. Furthermore, several defects can be observed at the edges and interiors of the heterointerface, including lattice distortions and site defects (Fig. S1, Supplementary data). The nano-heterostructures exposed on the surface of the electrocatalyst are helpful to increase the lattice defects, which subsequently produce abundant active sites to promote electrocatalytic activity and it is easier to adsorb intermediate in OER [8,34]. The selected-area electron diffraction (SAED) pattern, as demonstrated in Fig. S2 (Supplementary data), further validate the mixed feature of Ru, RuO$_2$ and Mn$_3$O$_4$ in Ru-RuO$_2$/Mn$_3$O$_4$/CP, in which well-resolved concentric rings (from inside to outside) are indexed to the (100) planes of Ru, the (110) and (101) planes of RuO$_2$, as well as the (105) planes of Mn$_3$O$_4$. The high angle annular dark field scanning transmission electron microscopy (HAADF-STEM) image and the corresponding elemental mapping results (Fig. 1c) display the Mn and O elements are uniformly distributed in the electrocatalyst with the relatively fewer Ru elements, demonstrating that Ru species are highly dispersed on Mn$_3$O$_4$. Therefore, Mn$_3$O$_4$ is the dominant body of the electrocatalyst composition, which supports Ru-RuO$_2$ nano-heterostructures to promote OER in acidic media. The SEM image in Fig. S3 (Supplementary data) shows that the bulky particles are unevenly anchored on carbon paper. All samples are connected tightly without obvious cracks, especially Ru-RuO$_2$/Mn$_3$O$_4$/CP shows a smooth surface. Following the OER reaction, the morphology of the samples also demonstrates virtually the same shape that are in the fresh state, suggesting that the samples have outstanding physical stability during OER reaction. In order to avoid the interference of the strong characteristic peaks of the carbon paper that disturbs the phase of the catalyst composition (Fig. S4, Supplementary data), electrocatalyst powders obtained under the same experimental conditions with the absence of carbon paper are conducted for X-ray diffraction (XRD) measurement. Moreover, following a series of controlled testing, we ultimately determined that 400 °C was the optimal calcination temperature for precursor (Fig. S5, Supplementary data). As depicted in Fig. 1d, the XRD pattern displays the crystallographic information of Mn$_3$O$_4$, RuO$_2$, and Ru. The MnCl$_2$ precursor was oxidized to the tetragonal Mn$_3$O$_4$ (PDF # 24–0734) after 6 h calcination at 400 °C. Alternatively, the corresponding XRD pattern presents the tetragonal RuO$_2$ (PDF # 88–0286) and hexagonal Ru (PDF # 06–0663) in the absence of manganese precursor, which suggests the incomplete oxidation of RuCl$_3$. As a result, the Ru-RuO$_2$/Mn$_3$O$_4$ contains characteristic peaks of three phases, which were synthesized by introducing ruthenium and manganese precursors together into the impregnation solution approach. Besides, the FWHM of (110), (101), and (211) crystal facets for RuO$_2$ in Ru-RuO$_2$/Mn$_3$O$_4$ are larger than those in Ru-RuO$_2$, indicating a smaller particle size of RuO$_2$ in Ru-RuO$_2$/Mn$_3$O$_4$ according to the Debye--Scherrer's equation. This is expected to expose more active sites, that are beneficial to catalytic activity [35]. To determine the mass loading of Ru and Mn on the carbon paper, results from inductively coupled plasma mass spectrometry (ICP-MS) show that the content ratio of Ru to Mn is about 1:6 in Ru-RuO$_2$/Mn$_3$O$_4$/CP (Table S1, Supplementary data). In addition, the structural characterization of Ru-RuO$_2$/CP (Fig. S6, Supplementary data) exhibits two well-defined lattice fringes, which are assigned to the (100) plane of Ru and the (110) plane of RuO$_2$, respectively. It is worth noting that there are two clear interface boundaries (white dashed line) exist between Ru and RuO$_2$, indicating the formation of the Ru-RuO$_2$ heterointerface. Likewise, various defects can be found at the heterointerface's edges and interiors, such as lattice distortions and site defects, which are similar to the interfacial characteristic of Ru-RuO$_2$/Mn$_3$O$_4$/CP. These interfaces with lots of defects would
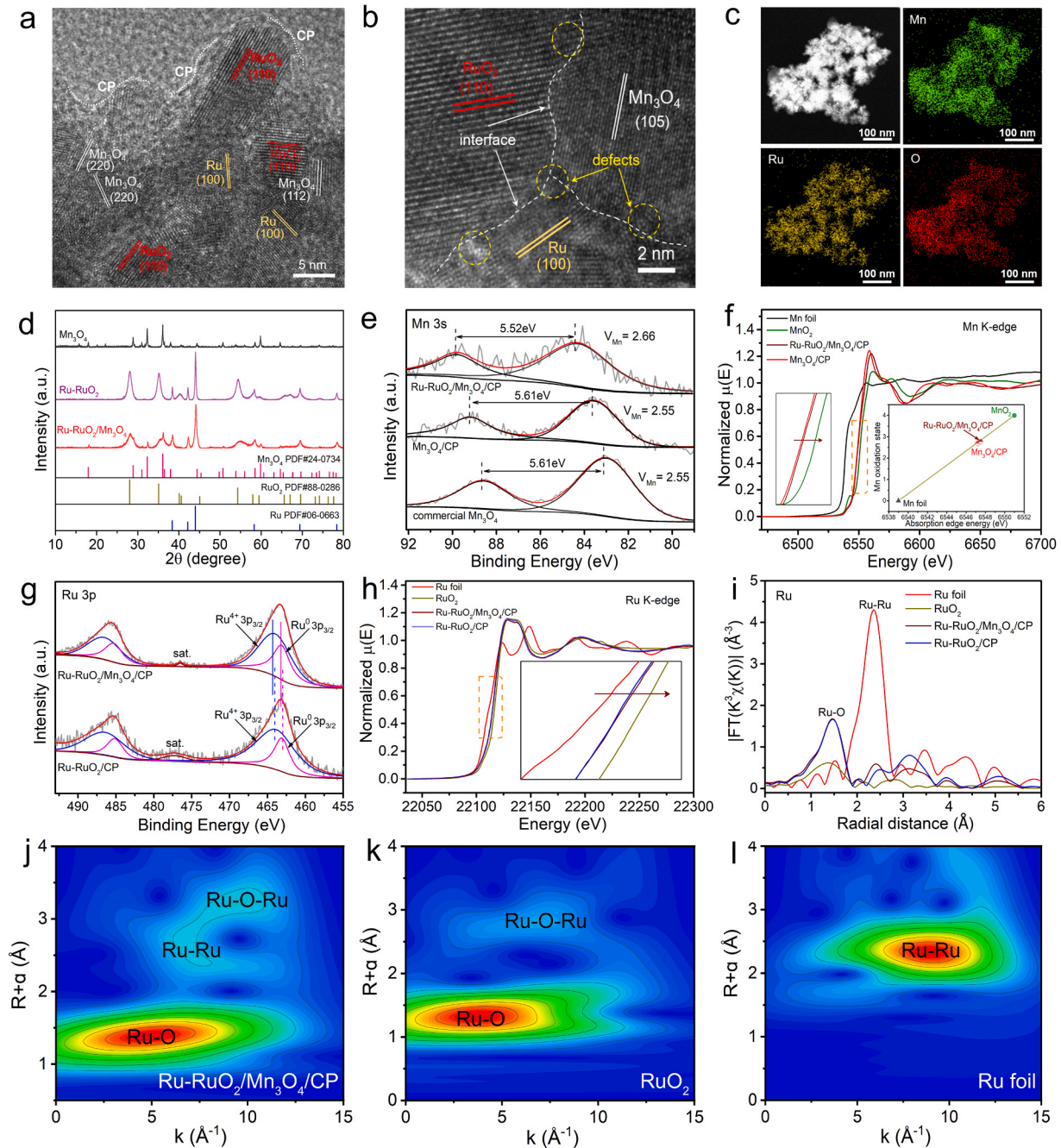
Fig. 1. Structural characterization of Ru-RuO$_2$/Mn$_3$O$_4$/CP. (a) TEM image; (b) HRTEM image; (c) HAADF-STEM image and elemental mappings of Mn, Ru, and O; (d) Powder X-ray diffraction patterns; (e) Mn 3 s XPS spectrum; (f) Normalized XANES spectra of Mn foil, MnO$_2$, Ru-RuO$_2$/Mn$_3$O$_4$/CP, and Mn$_3$O$_4$/CP, the bottom right inset: the relationship of Mn oxidation state vs. adsorption edge energy for above samples at the Mn K-edge; (g) Ru 3p XPS spectrum; (h) Normalized XANES and (i) EXAFS spectra of Ru foil, RuO$_2$, Ru-RuO$_2$/Mn$_3$O$_4$/CP, and Ru-RuO$_2$/CP at the Ru K-edge. Wavelet transforms for the k^2-weighted Ru K-edge EXAFS signals of (j) Ru-RuO$_2$/Mn$_3$O$_4$/CP, (k) RuO$_2$, and (l) Ru foil.

significantly increase the number of critical active sites, which would enhance electrocatalytic performance. The corresponding selected area electron diffraction (SAED) pattern (Fig. S7, Supplementary data) further demonstrates the mixed polycrystalline nature with distinct diffraction rings belonging to Ru and RuO$_2$. These interfaces with lots of defects would significantly increase the number of critical active sites, which would enhance electrocatalytic performance. Interestingly, the TEM image of Mn$_3$O$_4$/CP (Fig. S8, Supplementary data) exhibits the parallel and regular lattice fringes of Mn$_3$O$_4$ (200) with corresponding fast Fourier transform (FFT) pattern, which indicates that the applied calcination temperature and holding time are favorable for

crystallization of Mn$_3$O$_4$ rather than forming other manganese oxides of polymorphs.

X-ray photoelectron spectroscopy (XPS) measurements are qualified for investigating the electronic structure of the fresh electrocatalysts (Ru-RuO$_2$/Mn$_3$O$_4$/CP, Ru-RuO$_2$/CP, and Mn$_3$O$_4$/CP) before acidic OER. The Mn 2p$_{3/2}$ spectra in Fig. S9 and Table S2 (Supplementary data) show that three deconvoluted curves at 641.00, 642.10, and 644.40 eV correspond to Mn^{2+}, Mn^{3+}, and Mn^{4+} oxidation states of Ru-RuO$_2$/Mn$_3$O$_4$/CP, respectively [36,37]. Compared with Mn$_3$O$_4$/CP and commercial Mn$_3$O$_4$, the binding energy of manganese's valence state in Ru-RuO$_2$/Mn$_3$O$_4$/CP has shifted to the positive direction, which is

attributed to the influence of the load of Ru-RuO$_2$ nano-heterostructures. According to the literature, the Mn 3 s exchange splitting $\Delta E_{3\,s}$ is used to determine Mn valences (V_{Mn}) by the linear equation: V_{Mn} = 9.67–1.27$\Delta E_{3\,s}$ [38,39]. As shown in Fig. 1e, the average valence states of Mn in the Ru-RuO$_2$/Mn$_3$O$_4$/CP and Mn$_3$O$_4$/CP are 2.66 ($\Delta E_{3\,s}$ =5.52 eV) and 2.55 ($\Delta E_{3\,s}$ =5.61 eV) respectively, which are close to the average valence in commercial Mn$_3$O$_4$. To further assess the Mn valences in Ru-RuO$_2$/Mn$_3$O$_4$/CP, the normalized spectra of X-ray absorption near-edge structure (XANES) spectra at the Mn K-edge of samples are analyzed. Fig. 1f shows the absorption edge of Ru-RuO$_2$/Mn$_3$O$_4$/CP and Mn$_3$O$_4$/CP is located between Mn foil and commercial MnO$_2$, suggesting its valence between 0 and + 4. But the absorption edge of Ru-RuO$_2$/Mn$_3$O$_4$/CP shifts to the higher energy (left inset of Fig. 1f), which means that the Mn atoms in the Ru-RuO$_2$/Mn$_3$O$_4$/CP have the higher valence state than those in Mn$_3$O$_4$/CP. Based on the calculated valence states in the bottom right inset of Fig. 1f, the average valence of Mn atoms in the Ru-RuO$_2$/Mn$_3$O$_4$/CP and Mn$_3$O$_4$/CP are approximately + 2.77 and + 2.69, which is closely consistent with the XPS results [20]. The sequential valence gradient (Mn^{2+}/ Mn^{3+}/ Mn^{4+}) and a wide range of Mn-O bond length in Mn$_3$O$_4$ substrate are expected to operate as an effective sacrificial component, reducing the driving force for Ru-RuO$_2$ nano-heterostructures dissolution [36]. The extended X-ray absorption fine structure (EXAFS) with Fourier transform is performed to study the radial distribution function (RDF) of Mn atoms in Fig. S6, the fresh Ru-RuO$_2$/Mn$_3$O$_4$/CP shows stronger intensity corresponding to the Mn-O bond first coordination shell in comparison to Mn$_3$O$_4$/CP. However, the secondary coordination peak can be designated as the Mn-O-Mn bond of Ru-RuO$_2$/Mn$_3$O$_4$/CP, which is weaker and shorter than that of Mn$_3$O$_4$/CP, suggesting the distorted coordination environment around the Mn center due to the interactive coupling with Ru-RuO$_2$ heterostructures.

Further XPS analyses for both Ru-RuO$_2$/Mn$_3$O$_4$/CP and Ru-RuO$_2$/CP are applied to deeply understand the interaction of electrons between Ru and RuO$_2$. Consequently, the Ru 3p XPS spectra is given in Fig. 1g. Four peaks are deconvoluted in the high-resolution Ru 3p XPS spectrum for Ru-RuO$_2$/Mn$_3$O$_4$/CP, where the two peaks at 463.91 and 486.47 eV are respectively indexed to Ru 3p$_{3/2}$ and Ru 3p$_{1/2}$ of Ru (IV), and those at 463.11 and 485.27 eV could be assigned to Ru 3p$_{3/2}$ and Ru 3p$_{1/2}$ of Ru (0) [17,40]. It is observed that the Ru 3p spectra for Ru-RuO$_2$/Mn$_3$O$_4$/CP slightly shifts to the higher binding energies relative to the Ru 3p of Ru-RuO$_2$/CP, giving the differences of 0.09 eV and 0.03 eV for Ru (IV) 3p$_{3/2}$ and Ru (0) 3p$_{3/2}$, respectively (Table S3, Supplementary data). According to previous studies [19,41], the Ru species with a higher oxidation state in the Ru-based electrocatalysts could enhance the OER activity. This implies the Ru species in Ru-RuO$_2$/Mn$_3$O$_4$/CP is more active than Ru-RuO$_2$/CP, probably as a result of the presence of the Mn$_3$O$_4$ substrate that may lead to effective interfacial charge transfer. Interestingly, both the Ru and Mn element in Ru-RuO$_2$/Mn$_3$O$_4$/CP shift positively compared to Ru-RuO$_2$/CP and Mn$_3$O$_4$/CP, respectively, suggesting strong electron interactions between Ru-RuO$_2$ and Mn$_3$O$_4$ [42–44].

The high-resolution O 1 s spectra of Ru-RuO$_2$/Mn$_3$O$_4$/CP (Fig. S9, Supplementary data) exhibits four deconvoluted peaks at 529.8 eV, 530.3 eV, 531.9 eV, and 533.1 eV, which belong to Ru-O, Mn-O, surface adsorption oxygen (O$_{ads}$), and adsorbed water (H$_2$O$_{ads}$) [40,45,46]. Fig. 1h presents the normalized Ru K-edge XANES spectra, in which the RuO$_2$, Ru-RuO$_2$/Mn$_3$O$_4$/CP, and Ru-RuO$_2$/CP all display similar absorption edge and post-edge oscillations. In addition, the peak intensities of corresponding white-lines are sharply higher than that of reference Ru foil, which suggests rather higher chemical states of the Ru atoms in those three samples. It is observed that the absorption edges of Ru-RuO$_2$/Mn$_3$O$_4$/CP and Ru-RuO$_2$/CP locate between the reference Ru foil and commercial RuO$_2$. This indicates that the averaged Ru valence falls in the value of 0–4, which can be ascribed to the formation of Ru-RuO$_2$ nano-heterostructures. However, compared to Ru-RuO$_2$/CP, a positive shift in the absorption edge can be observed for the Ru-RuO$_2$/Mn$_3$O$_4$/CP

(inset of Fig. 1h), demonstrating that the introduction of Mn$_3$O$_4$ substrate results in the valent increase of Ru. The results of Ru K-edge XANES are also in accordance with the Ru 3p XPS results. The corresponding extended X-ray absorption fine-structure (EXAFS) spectrum of Ru-RuO$_2$/Mn$_3$O$_4$/CP and Ru-RuO$_2$/CP at the Ru K-edge show a dominant peak at around 1.47 Å (Fig. 1i), in accordance with the first coordination shell of Ru-O scattering path, which is larger than RuO$_2$ (≈1.38 Å). This signifies that the formation of Ru-RuO$_2$ nano-heterostructures is followed by a modest variation in the length of the Ru-O bond. In addition, the peak intensity of Ru-Ru bond first scattering interaction located at around 2.41 Å and 2.46 Å in the Ru-RuO$_2$/Mn$_3$O$_4$/CP and Ru-RuO$_2$/CP are lower than that of Ru-O bond, which means the number of Ru-Ru bond is fewer than Ru-O bond.

Wavelet transformations (WT) were used to further investigate the Ru-O and Ru-Ru coordination environment in Ru-RuO$_2$/Mn$_3$O$_4$/CP. The WT maximum for the pronounced Ru-O scattering path ($\sim$ 5.0 Å^{-1}, Fig. 1j) in Ru-RuO$_2$/Mn$_3$O$_4$/CP is larger than that in the RuO$_2$ ($\sim$ 4.1 Å^{-1}, Fig. 1k), indicating that the Ru element in Ru-O scattering interaction is partially replaced by the heavier element of Ru/Mn to form a portion of Ru-Ru/Ru-Mn scattering interaction [47–49]. Similarly, one sub-center located at $\sim$ 9.6 Å^{-1} is ascribed to the Ru-O-Ru coordination for Ru-RuO$_2$/Mn$_3$O$_4$/CP, which is larger than that in the RuO$_2$ ($\sim$ 7.5 Å^{-1}). Furthermore, the other sub-center situated at $\sim$ 7.2 Å^{-1} is assignable to the Ru-Ru coordination for Ru-RuO$_2$/Mn$_3$O$_4$/CP, whose intensity is weaker than that of Ru foil ($\sim$ 8.9 Å^{-1}, Fig. 1l). Since Ru-RuO$_2$ nano-heterostructures are loaded on the Mn$_3$O$_4$ substrate, the Ru-Ru scattering interaction is partially substituted by the lighter element of Mn, resulting in the shorter sub-center. In a nutshell, XPS and XAFS characterization results provide clear evidence of the formation of the Ru-RuO$_2$ nano-heterostructures combined with the multivalent Mn$_3$O$_4$ substrate.

3.2. Acidic OER performance

The OER performance of these prepared electrocatalysts in O$_2$-saturated 0.5 M H$_2$SO$_4$ was investigated by using a standard three-electrode configuration. For comparison's sake, commercial RuO$_2$ and Ru/C electrocatalysts were also investigated under the same conditions. Typically, the electrocatalytic activity was measured by the linear sweep voltammetry (LSV) method (Fig. 2a). It can be clearly observed that Ru-RuO$_2$/Mn$_3$O$_4$/CP exhibits the lowest overpotential at 10 mA cm^{-2} (η_{10} = 182 mV) than that of Ru-RuO$_2$/CP (η_{10} = 217 mV), Mn$_3$O$_4$/CP (η_{10} = 289 mV), and commercial RuO$_2$ (η_{10} = 295 mV). Interestingly, the commercial Ru/C exhibits a gradually increased anodic current response at the beginning of the LSV scan, which also shows a similar onset potential to Ru-RuO$_2$/Mn$_3$O$_4$/CP in appearance, but it should be attributed to the phenomenon that the metallic Ru itself is easily oxidized [50]. The corresponding Tafel analysis exhibits that the Ru-RuO$_2$/Mn$_3$O$_4$/CP reaches the smallest slope of 97.4 mV dec^{-1} (Fig. S12, Supplementary data) compared with the Ru-RuO$_2$/CP (164.5 mV dec^{-1}), commercial RuO$_2$ (141.7 mV dec^{-1}), and Mn$_3$O$_4$/CP (372.9 mV dec^{-1}), suggesting the fastest OER kinetics and electron transfer occur on the defect-rich surface of Ru-RuO$_2$/Mn$_3$O$_4$/CP among various electrocatalysts. Particularly, the result in Fig. 2b shows that Ru-RuO$_2$/Mn$_3$O$_4$/CP could reach a remarkable mass activity of 1324.6 A g$_{Ru}^{-1}$ (normalized by Ru) at 1.50 V vs. RHE, which is roughly 110.4 times and 10.7 times higher than those of commercial RuO$_2$ (12 A g$_{Ru}^{-1}$) and commercial Ru/C (123.3 A g$_{Ru}^{-1}$). Most importantly, compared with commercial electrocatalysts, such an excellent OER performance.

of Ru-RuO$_2$/Mn$_3$O$_4$/CP can be obtained directly on carbon paper with a loading mass of only 42.2 μg Ru precious metal.

The electrochemical impedance spectroscopy (EIS) from 100 kHz to 0.01 kHz for all electrocatalysts is performed to further explore the difference of catalytic kinetics. In general,

three components including double-layer capacitance, charge-transfer resistance, and solution resistance exist in Nyquist plots
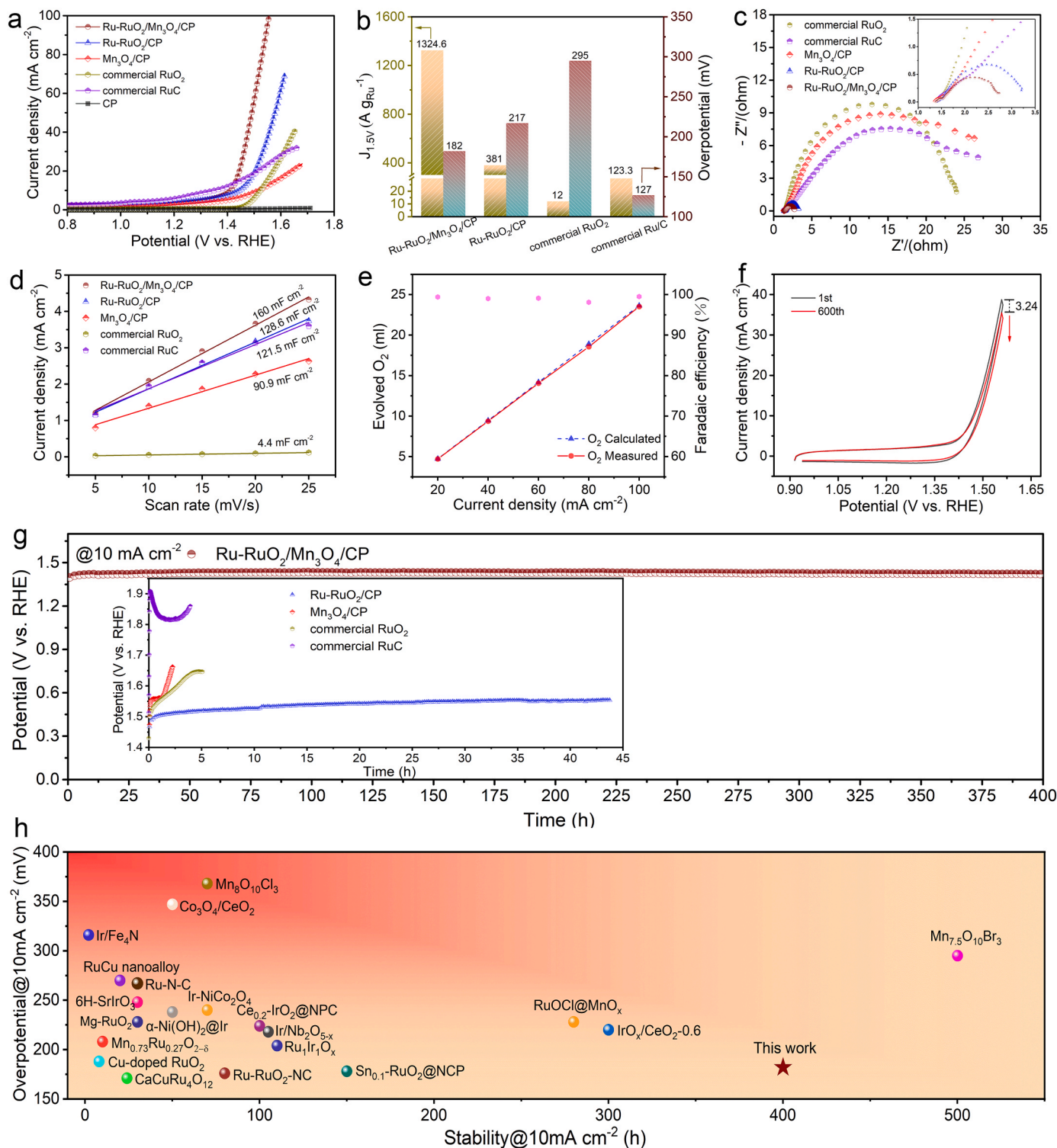
Fig. 2. Electrocatalytic OER performance. (a) LSV curves with iR-correction of various electrocatalysts in 0.5 M H$_2$SO$_4$; (b) Overpotentials at 10 mA cm^{-2} and normalized mass activities at 1.50 V vs. RHE of Ru-RuO$_2$/Mn$_3$O$_4$/CP, Ru-RuO$_2$/CP, commercial RuO$_2$, and commercial Ru/C; (c) Nyquist plots at 1.50 V vs. RHE of various catalysts; (d) C$_{dl}$ of various catalysts; (e) The FE of Ru-RuO$_2$/Mn$_3$O$_4$/CP. (f) CV cycles of Ru-RuO$_2$/Mn$_3$O$_4$/CP; (g) Chronopotentiometry curves at 10 mA cm^{-2} for Ru-RuO$_2$/Mn$_3$O$_4$/CP and the other electrocatalysts inset; (h) Comparison of OER activity for various reported electrocatalysts (Table S5, Supplementary data), the x and y axes represent the stability and overpotential at 10 mA cm^{-2}, respectively.

(Fig. S13, Supplementary data). As shown in Fig. 2c, there are two semicircle curves, where the high frequency resistance can be employed to determine the charge transfer resistance (R$_{ct}$) relevant to electrocatalytic kinetics, and the low frequency resistance can be used to efficiently measure transmit electronic signals at the interfaces between

electrodes and electrolytes [51]. At the potential of 1.50 V vs. RHE, all the samples exhibit similar large semicircles, corresponding to the dramatic OER process [52]. Consequently, the results present that the semicircles for both Ru-RuO$_2$/Mn$_3$O$_4$/CP and Ru-RuO$_2$/CP are much smaller than those for other samples mentioned above, implying that the

built-in Ru-RuO₂ nano-heterostructures contribute to the formation of electronic transport channels at Ru|RuO₂ interfaces and it thus effectively accelerate the OER kinetics [23,53,54]. Notably, the Ru-RuO₂/Mn₃O₄/CP possesses the minimum R_{ct} of only 1.26 Ω among all samples, indicating that the introduction of Mn₃O₄ substrate can further promote electron transfer at the interface so as to achieve its fastest OER dynamics. Additionally, cyclic voltammetry experiments were carried out at various scan speeds in the non-Faraday region to acquire C_{dl} for estimation of the relative electrochemically active surface area (Fig. S14, Supplementary data) [55]. Fig. 2d shows that the C_{dl} value of Ru-RuO₂/Mn₃O₄/CP (160 mF cm⁻²) are higher than Ru-RuO₂/CP (128.6 mF cm⁻²), commercial Ru/C (121.5 mF cm⁻²), Mn₃O₄/CP (90.9 mF cm⁻²), and commercial RuO₂ (4.4 mF cm⁻²), suggesting that the

Ru-RuO₂ nano-heterostructures loaded on Mn₃O₄ substrate possess more active sites and thus boost acidic OER performance. The water displacement method was implemented to calculate the Faradaic efficiency (FE) of OER (Fig. S15, Supplementary data) [46]. The outcome in Fig. 2e demonstrates that under various current densities, the measured oxygen volume approaches 100% FE and agrees well with the theoretical values calculated by Faraday's law of electrolysis.

The durability of the Ru-RuO₂/Mn₃O₄/CP under harsh acidic conditions is another critical criterion for practical applications. Compared with the Ru-RuO₂/CP and commercial RuO₂ (Fig. S16, Supplementary data), the Ru-RuO₂/Mn₃O₄/CP shows a slight degradation of 3.24 mA cm⁻² after 600 cyclic voltammogram cycles (CV) in the range from 0.91 V to 1.56 V vs. RHE (Fig. 2f). Additionally, these as-prepared
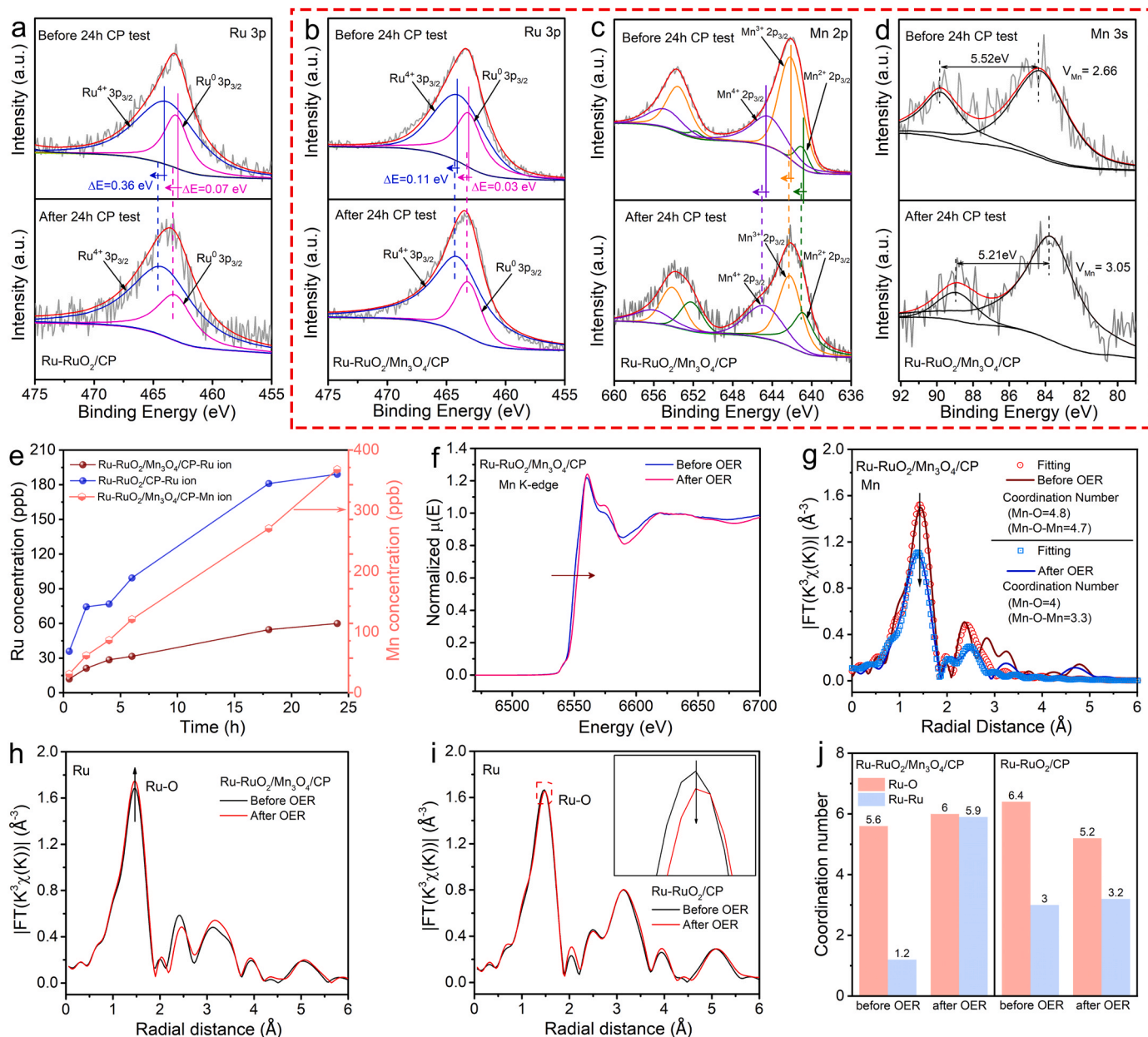

Fig. 3. Electronic and atomic structure changes before and after OER. High-resolution XPS spectra of (a) Ru 3p₃/₂ for Ru-RuO₂/CP before and after 24 h CP test at 10 mA cm⁻²; High-resolution XPS spectra of (b) Ru 3p₃/₂ (c) Mn 2p and (d) Mn 3 s for Ru-RuO₂/Mn₃O₄/CP before and after 24 h CP test at 10 mA cm⁻²; (e) Concentration of dissolved Ru and Mn ion in electrolyte during 24 h CP test; (f) Normalized XANES spectra at the Mn K-edge for Ru-RuO₂/Mn₃O₄/CP before and after the OER test; (g) The R-space curve-fitting curves in the Mn K-edge for Ru-RuO₂/Mn₃O₄/CP before and after OER; R-space of the EXAFS spectra at the Ru K-edge for (h) Ru-RuO₂/Mn₃O₄/CP and (i) Ru-RuO₂/CP before and after the OER test; (j) The coordination number of Ru-O and Ru-Ru for Ru-RuO₂/Mn₃O₄/CP and Ru-RuO₂/CP before and after the OER test.

OER electrocatalysts are investigated by chronopotentiometry (CP) test at 10 mA cm^{-2}, which is recommended as a widely adapted benchmark OER stability testing condition [56,57]. As depicted in Fig. 2g, it is noteworthy that Ru-RuO$_2$/Mn$_3$O$_4$/CP remains a quite steady performance for the 400 h CP test, implying its outstanding long-term stability for acidic OER. By contrast, commercial RuO$_2$, commercial Ru/C, and as-synthesized Mn$_3$O$_4$/CP exhibit rapid activity decays during the OER stability test. Although the as-synthesized Ru-RuO$_2$/CP shows a relatively slow decay at 10 mA cm^{-2} for more than 40 h in the inset of Fig. 2g, the stability in Ru-RuO$_2$/CP decreases faster with the increase of current density (Fig. S17–19, Supplementary data). The superior OER stability of Ru-RuO$_2$/Mn$_3$O$_4$/CP clearly emphasizes the critical role of Mn$_3$O$_4$ substrate. To summarize, Fig. 2h and Table S5 (Supplementary data) show a comparison of the performance of Ru-RuO$_2$/Mn$_3$O$_4$/CP with previously reported acidic OER electrocatalysts in activity and stability, evidently indicating that Ru-RuO$_2$/Mn$_3$O$_4$/CP exhibits considerable OER performance in the 0.5 M H$_2$SO$_4$ electrolyte comparatively, outperforming other recently reported noble metal-based electrocatalysts.

3.3. Exposition of the sacrificing oxidation strategy of Mn$_3$O$_4$ substrate

To shed light on the protective mechanism of Mn$_3$O$_4$ substrate against Ru-RuO$_2$ nano-heterostructures, we investigated the electronic structural change of Ru-RuO$_2$/Mn$_3$O$_4$/CP and Ru-RuO$_2$/CP before and after the acidic OER process. It is known that the process of longstanding current input and continuous adsorption and desorption of intermediates (H$_2$O, OH*, O*, and OOH*) is the ordeal for electrocatalysts lifetime, which is also accompanied with excessive oxidation and dissolution of metal active center ions (Ru$^{\delta>4+}$). Hence, determining the oxidation degree of Ru ions before and after the stability test is necessary to evaluate their antioxidant ability. As exhibited in the XPS spectrum of Fig. 3a, the Ru 3p$_{3/2}$ in Ru-RuO$_2$/CP after 24 h chronopotentiometry test at 10 mA cm^{-2} presents a higher oxidation state than that in the fresh Ru-RuO$_2$/CP, which displays the positive shifts of 0.36 and 0.07 eV toward the high binding energy for Ru (IV) 3p$_{3/2}$ and Ru (0) 3p$_{3/2}$, respectively. The decrease of Ru (0) 3p$_{3/2}$ proportion implies that some Ru^{4+} species in the heterostructures is over-oxidized and dissolved into the electrolyte, at the same time, the adjacent metallic Ru is partially oxidized to Ru^{4+} as a supplement source. In comparison, the Ru-RuO$_2$/Mn$_3$O$_4$/CP shows the positive shifts of only 0.11 and 0.03 eV for Ru (IV) 3p$_{3/2}$ and Ru (0) 3p$_{3/2}$ after 24 h stability test (Fig. 3b), evidencing that the introduction of Mn$_3$O$_4$ substrate can suppress the over-oxidation of the Ru species, which contributes to the highly improved antioxidant ability and stability of Ru-RuO$_2$ nano-heterostructures. Varied degrees of positive energy shift of Mn^{2+}, Mn^{3+}, and Mn^{4+} in Ru-RuO$_2$/Mn$_3$O$_4$/CP can be observed for Ru-RuO$_2$/Mn$_3$O$_4$/CP in Fig. 3c, in detail, it can be found in Fig. 3d that the average valence of Mn species in Mn 3 s spectra increases to 3.05 from 2.66 after stability test.

In addition, the TEM image (Fig. S20 a, Supplementary data) further confirms that the highly dispersed Ru-RuO$_2$ nano-heterostructures primary grains are anchored in the Mn$_3$O$_4$ substrate without reconstruction or aggregation after 150 h′ stability test, and the corresponding elemental mapping also confirms that Ru, Mn, and O atoms still exist in Ru-RuO$_2$/Mn$_3$O$_4$/CP, but there are fewer Ru and Mn atoms than the pristine state for all cases of comparison electrocatalysts, denoting that the metal ions of Ru-RuO$_2$/Mn$_3$O$_4$/CP more tardily dissolve in electrolyte during a long stability test. This result demonstrates that the excellent stability of Ru-RuO$_2$/Mn$_3$O$_4$/CP is benefited from the synergistic effect between Mn$_3$O$_4$ substrate and Ru-RuO$_2$ nano-heterostructures. Comparatively, Mn$_3$O$_4$ is more susceptible to oxidation than Ru and RuO$_2$ under large overpotential in the OER range, which consequently protects Ru species from over-oxidation and guarantees the stable existence of active sites in Ru-RuO$_2$/Mn$_3$O$_4$/CP.

Time-dependent Ru ion dissolution results in Fig. 3e can further reflect the importance of Mn$_3$O$_4$ substrate. In order to monitor the

dissolution of the noble metal, we measured Ru ion dissolution in the electrolyte during 24 h CP test at 10 mA cm^{-2} via ICP-MS (Table S6, Supplementary data). The histogram discloses that the dissolution amount of Ru ion in Ru-RuO$_2$/CP is larger than that in Ru-RuO$_2$/Mn$_3$O$_4$/CP during the same time, suggesting that Ru ion is leached out of the Ru-RuO$_2$/CP rapidly during the stability test. Besides, the Ru dissolution rate of Ru-RuO$_2$/CP in the absence of Mn$_3$O$_4$ substrate becomes faster with the increase of testing time. In terms of the RuO$_2$/Mn$_3$O$_4$/CP, Ru ion dissolves slowly, whereas the dissolved Mn ion experiences a gradual rise. The dissolution ratio of the Ru element in Ru-RuO$_2$/Mn$_3$O$_4$/CP after 24 h is only 60 ppb, which is approximately one-third of the dissolution ratio in Ru-RuO$_2$/CP, while the Mn element's dissolution ratio is 368.1 ppb. Full range spectrum results of XPS further confirm the remained Ru in the two samples after the stability test (Fig. S21, Supplementary data). The dramatically weakened peak intensities of Ru 3p and 3d in Ru-RuO$_2$/CP indicate a large amount of Ru ion dissolution, which is in accordance with the results of ICP-MS. In contrast to Ru-RuO$_2$/CP, the Ru 3p and 3d peak intensities do not decrease distinctly in Ru-RuO$_2$/Mn$_3$O$_4$/CP. Alternatively, the peak intensity of Mn 2p is weakened significantly, implying that cost-effective Mn atoms are sacrificed to protect noble Ru atoms. Therefore, we conjecture that the sacrificing oxidation of the Mn$_3$O$_4$ substrate is capable of stabilizing the entire electrocatalyst by decreasing the driving force of dissolution of Ru-RuO$_2$.

Moreover, the important role of Mn$_3$O$_4$ substrate is also indicated by the ex-situ XANES.

spectra for the Ru-RuO$_2$/CP and Ru-RuO$_2$/Mn$_3$O$_4$/CP electrocatalysts before and after OER. Fig. 3f demonstrates that the OER process increases the valence state of Mn species in Ru-RuO$_2$/Mn$_3$O$_4$/CP while only slightly increasing the valence state of Ru species (Fig. S22 a, Supplementary data). The slight positive shift of the Ru K-edge indicates the positive accumulation of Ru^{4+} species (i.e. RuO$_2$) in Ru-RuO$_2$/Mn$_3$O$_4$/CP, which is beneficial to the electrocatalytic activity and stability in harsh acidic environment [58]. However, the Ru K-edge in Ru-RuO$_2$/CP without the protection of Mn$_3$O$_4$ substrate shows an opposite shift after OER (Fig. S22 b, Supplementary data), namely, the decrease of valence state for Ru, implying that the dissolution rate of Ru ions is more predominant than the oxidation rate from metallic Ru to RuO$_2$. Furthermore, the coordination number (CN) obtained from EXAFS spectra exhibits the details of structural evolution (Table S7, Supplementary data). The R-space fitting curves in the Mn K-edge show that the CN of Mn-O decreases from 4.8 to 4, and the CN of Mn-O-Mn decreases from 4.7 to 3.3, suggesting the dissolution of Mn atoms after OER (Fig. 3g and Fig. S23, Supplementary data). The sacrificial dissolution of the Mn$_3$O$_4$ substrate is further revealed by the negative shift of next nearest-neighbor (Mn-O-Mn) in Ru-RuO$_2$/Mn$_3$O$_4$/CP, which is supported by the WT results (Fig. S24, Supplementary data). Specifically, since the electronegativity of Mn (1.55) is lower than that of Ru (2.20), Ru atom has a tendency to acquire electrons from Mn via O bridge, and thus the Mn$_3$O$_4$ substrate can effectively alleviate the over-oxidation of Ru atoms to turn into soluble Ru$^{\delta>4+}$ species during OER [34,59]. The CNs' variation of Ru-O and Ru-Ru bonds are also investigated for the Ru-RuO$_2$/Mn$_3$O$_4$/CP and Ru-RuO$_2$/CP before and after acidic OER, and the results are given in Fig. 3h-j and Fig. S25–26 (Supplementary data). On one hand, the CN of Ru-O in Ru-RuO$_2$/Mn$_3$O$_4$/CP increases from 5.6 to 6, while such CN in Ru-RuO$_2$/CP decreases from 6.4 to 5.2 after OER. This is attributed to the probably existed O bridge between Ru and Mn. That is, the formation of Mn-O-Ru bonds could be the rationale behind this. Though the dissolution of metal Mn occurs in Ru-RuO$_2$/Mn$_3$O$_4$/CP during the reaction, the O bridge chemically interacted with adjacent Ru would be helpful to maintain the active valence state of Ru species for acidic OER. On the other hand, the CN of Ru-Ru in Ru-RuO$_2$/Mn$_3$O$_4$/CP considerably increases from 1.2 to 5.9, while such CN in Ru-RuO$_2$/CP slightly increases from 3 to 3.2. As validated by the WT results (Fig. S27–28, Supplementary data), the sub-center Ru-Ru bond in Ru-RuO$_2$/CP changes

insignificantly, whereas the area of the Ru-Ru bond in Ru-RuO$_2$/Mn$_3$O$_4$/CP clearly extend, indicating that the content of the Ru-Ru bond increases. It suggests that the Ru atoms on the Mn$_3$O$_4$ substrate would bond with each other after Mn ions dissolution, which can remit the dissolution of Ru atoms. These results reflect that the Mn$_3$O$_4$ substrate can effectively suppress the over-oxidation of Ru species in Ru-RuO$_2$/Mn$_3$O$_4$/CP during the violent oxygen evolution, highlighting the vital effect of sacrificing oxidation of Mn$_3$O$_4$ substrate.

3.4. Identification of OER mechanism

To further investigate the putative catalytic mechanism on commercial RuO$_2$, Ru-RuO$_2$/CP, and Ru-RuO$_2$/Mn$_3$O$_4$/CP, the pH-

dependence measurements of their OER activities were conducted in the pH range of 0.3–1 (Fig. 4a and Fig. S29 in Supplementary data). The commercial RuO$_2$ shows different OER performance in the electrolyte with different pH values, suggesting the participation of lattice oxygen in the acidic OER that is proceeded on RuO$_2$ surface [10]. In contrast to the commercial RuO$_2$, both Ru-RuO$_2$/CP and Ru-RuO$_2$/Mn$_3$O$_4$/CP exhibit negligible pH dependence. That is, their current densities are almost constant in different pH values under varied OER overpotentials. The results reveal that Ru-RuO$_2$/CP and Ru-RuO$_2$/Mn$_3$O$_4$/CP follow proton coupled electron transfer (PECT) process, which is consistent with the characteristics of the adsorbate evolution mechanism (AEM) [20,60]. The generation of oxygen via AEM pathway in acid electrolyte requires four protons and electrons, which can be separated into four
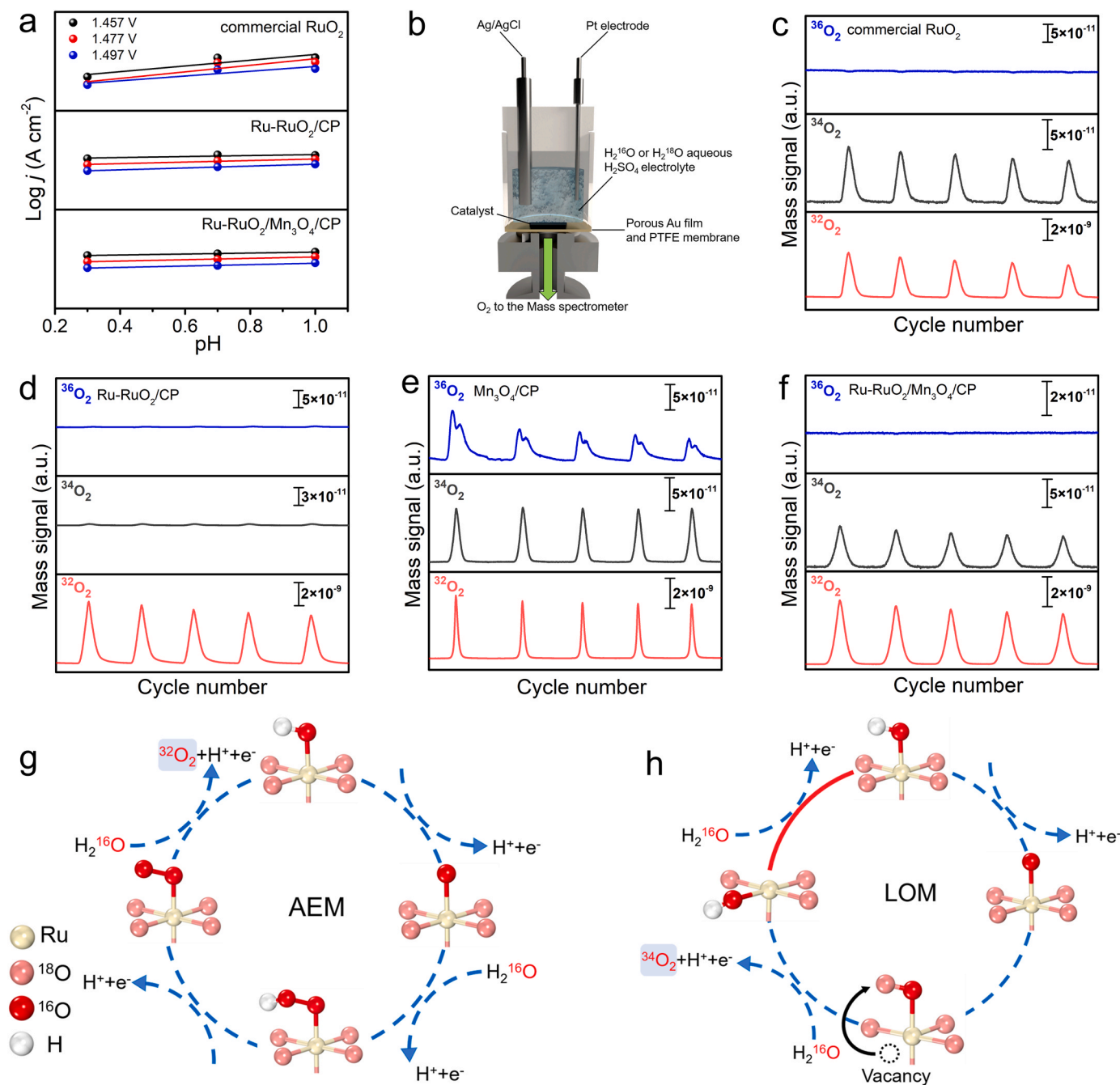

Fig. 4. OER mechanism analysis. (a) pH-independent OER activities for commercial RuO$_2$, Ru-RuO$_2$/CP, and Ru-RuO$_2$/Mn$_3$O$_4$/CP; (b) Schematic illustration of the *operando* DEMS; DEMS signals of $^{36}O_2$, $^{34}O_2$, and $^{32}O_2$ from the reaction products for ^{18}O-labeled (c) commercial RuO$_2$, (d) Ru-RuO$_2$/CP, (e) Mn$_3$O$_4$/CP and (f) Ru-RuO$_2$/Mn$_3$O$_4$/CP catalysts in H$_2^{16}$O aqueous H$_2$SO$_4$ electrolyte; Schematic illustration of (g) AEM and (h) LOM pathway for OER on the RuO$_2$ (110) surface.
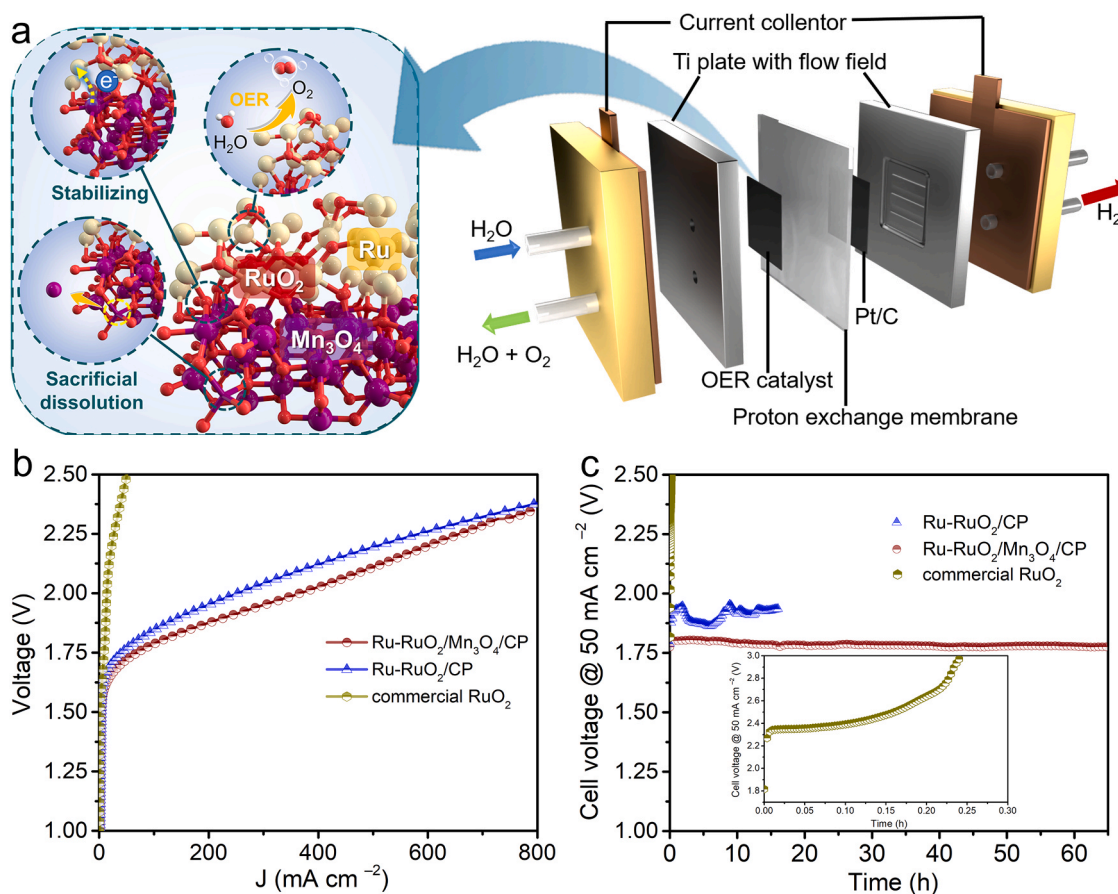
Fig. 5. PEM electrolyzer demonstration. (a) Schematic illustration of the sacrificing oxidation strategy of Mn_3O_4 substrate for $Ru-RuO_2$ nano-heterostructures and PEM electrolyzer device; (b) Polarization curves of a PEM electrolyzer measured at ambient temperature; (c) Chronopotentiometry tests at 50 mA cm^{-2} in the PEM electrolyzer measured at ambient temperature.

steps: 1) $H_2O \rightarrow OH^* + H+ + e-$; 2) $OH^* \rightarrow O^* + H+ + e-$; 3) $O^* + H2O \rightarrow OOH^* + H+ + e-$; 4) $OOH^* \rightarrow O_2 + H^+ + e^-$.[61] According to the literature [46,62], the formed OH* intermediates are electrophiles that can be identified by interacting with nucleophiles like methanol. As demonstrated in Fig. S30 (Supplementary data), the $Ru-RuO_2$/CP and $Ru-RuO_2$/Mn$_3O_4$/CP present smaller onset potentials than commercial RuO_2, signifying that the faster methanol oxidation reaction (MOR) and stronger adsorption capability of the OH* intermediate occur on the catalyst surface.

To experimentally track the AEM pathway, *operando* differential electrochemical mass.

spectrometry (DEMS) with isotope labeling was carried out (Fig. 4b). We labeled the catalyst surface with ^{18}O in 0.5 M H_2SO_4 using $H_2^{18}O$ as the supporting solution, and then we measured the evolved O_2 in a normal 0.5 M H_2SO_4 solution (see Methods in Supplementary data). The signals of $^{32}O_2$ and $^{34}O_2$ observed on commercial RuO_2 (Fig. 4c) indicate that the OER gaseous product is generated on RuO_2 through the AEM and LOM pathway, in accordance with predecessors' research. However, no obvious $^{34}O_2$ signal can be observed on the $Ru-RuO_2$/CP (Fig. 4d), suggesting that the formation of heterostructures can effectively suppress the participation of lattice oxygen and change the reaction pathway from LOM to AEM [11,63]. Furthermore, as shown in Fig. 4e, the Mn_3O_4/CP exhibits three different signals, because of the vulnerable Mn-O mentioned above, the result reflects the existence of three different OER reaction paths in Mn_3O_4/CP simultaneously. Notably, the signal intensity of $^{36}O_2$ and $^{34}O_2$ are far weaker than $^{32}O_2$, suggesting the AEM path is dominant. It's worth noting in Fig. 4f that the $Ru-RuO_2$/Mn$_3O_4$/CP shows a similar variation trend compared with commercial RuO_2, and a small quantity of $^{34}O_2$ signal is derived from the

Mn_3O_4 substrate. However, no visible $^{36}O_2$ signal is detected on $Ru-RuO_2$/Mn$_3O_4$/CP, which could be related to a decrease in the O-O coupling ability of the Mn_3O_4 substrate due to interfacial effect. In short, the $^{32}O_2$ ($^{16}O^{16}O$) and $^{34}O_2$ ($^{16}O^{18}O$) signals reflect AEM and LOM pathways (Fig. 4g-h), respectively [11,64]. The DEMS analysis, combined with the pH-dependence measurements, demonstrates that the OER proceeds via the AEM pathway on the $Ru-RuO_2$/CP and $Ru-RuO_2$/Mn$_3O_4$/CP, and the formation of $Ru-RuO_2$ heterostructures can effectively suppress the LOM pathway, leading to the boosted OER stability and activity under acidic condition.

The above experimental evidence shows that the $Ru-RuO_2$ heterostructures are the vital.

active centers of $Ru-RuO_2$/Mn$_3O_4$/CP. In order to build a model of the $Ru-RuO_2$ heterostructure, (110) crystal facet is selected for RuO_2 and (100) crystal facet is selected for Ru according to the HRTEM image. Afterwards, density functional theory (DFT) computations are conducted to analyze the partial density of states (PDOS) and the Gibbs free energies of $Ru-RuO_2$ heterostructure (Fig. S31a, Supplementary data) compared with RuO_2. The PDOS result demonstrates that the Ru 4d band center (ε_d(Ru)) versus the Fermi level is − 4.348 eV in RuO_2, while such value is 4.163 eV in $Ru-RuO_2$ heterostructure, indicating that the d-band center is closer to the Fermi level after heterogenization. The upshifting of the d-band center after heterogenization strengthens the adsorption of oxygen intermediates [58,65,66]. These results indicate the covalency of Ru-O bond is increased after heterogenization, which is thermodynamically favorable to O-O coupling on $Ru-RuO_2$ heterostructures and kinetically in favor of adsorbate oxygen evolution [10,16]. Based on the DEMS measurements, the Gibbs free energies of OER via AEM pathway are calculated on the optimized RuO_2 (110) and on the Ru^{4+} site on

Ru-RuO$_2$ heterostructure. The result in Fig. S31b - 33 (Supplementary data) shows that the formation of *OOH is the potential-determining step (PDS) for both RuO$_2$ and Ru-RuO$_2$. Such PDS requires an uphill energy gap of 1.711 eV on Ru-RuO$_2$ which is 0.659 eV less than that on RuO$_2$, suggesting the Ru-RuO$_2$ heterostructures exert significant influence on reducing the *OOH binding energy. As a result, the thermodynamic advantage of Ru-RuO$_2$ heterostructures over pure RuO$_2$ is therefore demonstrated.

3.5. Electrocatalysis practical application demonstration

Finally, in order to confirm the viability of Ru-RuO$_2$/Mn$_3$O$_4$/CP for larger-scale practical applications, a flow-type electrolysis system was assembled by using Ru-RuO$_2$/Mn$_3$O$_4$/CP, Ru-RuO$_2$/CP, and commercial RuO$_2$ as the anode as well as the commercial Pt/C (20 wt%) as the cathode and separated by a Nafion membrane (Fig. 5a and Fig. S34 in Supplementary data). The polarization curves (without iR correction) in Fig. 5b demonstrate an apparent improvement in cell performance while maintaining a constant cathode side preparation.

condition at ambient temperatures. Obviously, the cell performance of the Ru-RuO$_2$/Mn$_3$O$_4$/CP tested in the PEMWE is superior to that of the Ru-RuO$_2$/CP and commercial RuO$_2$. With its high catalytic activity, the Ru-RuO$_2$/Mn$_3$O$_4$/CP reaches a current density of 100 and 500 mA cm^{-2} at 1.787 and 2.111 V, respectively. However, to reach the same performances above, the Ru-RuO$_2$/CP needs higher potentials of 1.845 and 2.194 V, and the commercial RuO$_2$ has a slow dynamic growth trend that prevents it from growing faster than 100 mA cm^{-2} even at 2.5 V. Besides, upon applying a constant current of 50 mA cm^{-2} (Fig. 5c), the Ru-RuO$_2$/Mn$_3$O$_4$/CP electrolyzer can steadily work for more than 65 h. But the stability of the Ru-RuO$_2$/CP electrolyzer fluctuates greatly and commercial RuO$_2$ electrolyzer displays poor tolerance throughout the test. In consequence, the Ru-RuO$_2$/Mn$_3$O$_4$/CP electrolyzer possesses promising activity and stability of water electrolysis at ambient temperatures.

4. Conclusion

In summary, we demonstrate that the Ru-RuO$_2$/Mn$_3$O$_4$/CP catalyst exhibits significantly boosted activity with an overpotential of merely 182 mV at 10 mA cm^{-2}, accompanied with enhanced stability of 400 h for acidic OER. The improved catalytic stability is ascribed to the introduction of Mn$_3$O$_4$ substrate, which can protect active Ru^{4+} species in Ru-RuO$_2$ nano-heterostructures from over-oxidation, thus effectively alleviating the dissolution of Ru in acidic electrolytes via sacrificing the Mn$_3$O$_4$ substrate itself for preferential oxidation. Besides, the DEMS and DFT calculation results confirm that the formation of Ru-RuO$_2$ nano-heterostructures can effectively increase the d-band center of Ru and greatly suppress the LOM pathway, resulting in the enhanced OER activity Ru-RuO$_2$/Mn$_3$O$_4$/CP. This work provides not only a perspective on investigating the sacrificing oxidation strategy of Mn$_3$O$_4$ substrate for Ru-based electrocatalysts, but also the scientific evidence for the modulation of the OER pathway in Ru-RuO$_2$ nano-heterostructures.

CRediT authorship contribution statement

Xin Long: Conceptualization, Methodology, Validation, Formal analysis, Investigation, Writing - Original Draft. **Bin Zhao:** Conceptualization, Methodology, Validation, Resources, Writing - Review & Editing, Supervision, Project administration, Funding acquisition. **Qianqian Zhao:** Methodology, Formal analysis. **Xuexian Wu:** Validation, Software, Formal analysis. **Meng-Nan Zhu:** Resources, Software, Formal analysis. **Renfei Feng:** Resources, Software, Formal analysis. **Mohsen Shakouri:** Resources, Software, Formal analysis. **Yu Zhang:** Resources, Software, Formal analysis. **Jiujun Zhang:** Validation, Resources, Supervision. **Xinxin Xiao:** Validation, Resources, Supervision, Writing - Review & Editing. **Xian-Zhu Fu:** Conceptualization,

Methodology, Validation, Resources, Writing - Review & Editing, Visualization, Supervision, Project administration, Funding acquisition. **Jing-Li Luo:** Conceptualization, Methodology, Validation, Resources, Writing - Review & Editing, Visualization, Supervision, Project administration, Funding acquisition.

Declaration of Competing Interest

The authors declare that they have no known competing financial interests or personal relationships that could have appeared to influence the work reported in this paper.

Data Availability

Data will be made available on request.

Appendix A. Supporting information

Supplementary data associated with this article can be found in the online version at doi:10.1016/j.apcatb.2023.123559.

References

[1] S. Hu, S. Ge, H. Liu, X. Kang, Q. Yu, B. Liu, Low-dimensional electrocatalysts for acidic oxygen evolution: intrinsic activity, high current density operation, and long-term stability, Adv. Funct. Mater. 32 (2022), 2201726, https://doi.org/10.1002/adfm.202201726.

[2] L. An, C. Wei, M. Lu, H. Liu, Y. Chen, G.G. Scherer, A.C. Fisher, P. Xi, Z.J. Xu, C. H. Yan, Recent development of oxygen evolution electrocatalysts in acidic environment, Adv. Mater. 33 (2021), 2006328, https://doi.org/10.1002/adma.202006328.

[3] Z.Y. Wu, F.Y. Chen, B. Li, S.W. Yu, Y.Z. Finfrock, D.M. Meira, Q.Q. Yan, P. Zhu, M. X. Chen, T.W. Song, Z. Yin, H.W. Liang, S. Zhang, G. Wang, H. Wang, Non-iridium-based electrocatalyst for durable acidic oxygen evolution reaction in proton exchange membrane water electrolysis, Nat. Mater. 22 (2022) 100–108, https://doi.org/10.1038/s41563-022-01380-5.

[4] K. Sardar, E. Petrucco, C.I. Hiley, J.D. Sharman, P.P. Wells, A.E. Russell, R. J. Kashtiban, J. Sloan, R.I. Walton, Water-splitting electrocatalysis in acid conditions using ruthenate-iridate pyrochlores, Angew. Chem. Int. Ed. 53 (2014) 10960–10964, https://doi.org/10.1002/anie.201406668.

[5] C. Wei, S. Sun, D. Mandler, X. Wang, S.Z. Qiao, Z.J. Xu, Approaches for measuring the surface areas of metal oxide electrocatalysts for determining their intrinsic electrocatalytic activity, Chem. Soc. Rev. 48 (2019) 2518–2534, https://doi.org/10.1039/c8cs00848e.

[5] G. Wei, C. Wei, Z.F. Huang, C. Liu, L. Zeng, X. Wang, Z.J. Xu, A review on fundamentals for designing oxygen evolution electrocatalysts, Chem. Soc. Rev. 49 (2020) 2196–2214, https://doi.org/10.1039/c9cs00607a.

[6] I.C. Man, H.Y. Su, F. Calle-Vallejo, H.A. Hansen, J.I. Martínez, N.G. Inoglu, J. Kitchin, T.F. Jaramillo, J.K. Nørskov, J. Rossmeisl, Universality in oxygen evolution electrocatalysis on oxide surfaces, ChemCatChem 3 (2011) 1159–1165, https://doi.org/10.1002/cctc.201000397.

[7] T. Reier, H.N. Nong, D. Teschner, R. Schlögl, P. Strasser, Electrocatalytic oxygen evolution reaction in acidic environments - reaction mechanisms and catalysts, Adv. Energy Mater. 7 (2017), 160127, https://doi.org/10.1002/aenm.201601275.

[8] Y. Lin, Y. Dong, X. Wang, L. Chen, Electrocatalysts for oxygen evolution reaction in acidic media, Adv. Mater. 35 (2022), 221056, https://doi.org/10.1002/adma.202210565.

[9] Z.-F. Huang, J. Song, Y. Du, S. Xi, S. Dou, J.M.V. Nsanzimana, C. Wang, Z.J. Xu, X. Wang, Chemical and structural origin of lattice oxygen oxidation in Co–Zn oxyhydroxide oxygen evolution electrocatalysts, Nat. Energy 4 (2019) 329–338, https://doi.org/10.1038/s41560-019-0355-9.

[10] A. Grimaud, O. Diaz-Morales, B. Han, W.T. Hong, Y.L. Lee, L. Giordano, K. A. Stoerzinger, M.T.M. Koper, Y. Shao-Horn, Activating lattice oxygen redox reactions in metal oxides to catalyse oxygen evolution, Nat. Chem. 9 (2017) 457–465, https://doi.org/10.1038/nchem.2932.

[11] Y. Wen, P. Chen, L. Wang, S. Li, Z. Wang, J. Abed, X. Mao, Y. Min, C.T. Dinh, P. Luna, R. Huang, L. Zhang, L. Wang, L. Wang, R.J. Nielsen, H. Li, T. Zhuang, C. Ke, O. Voznyy, Y. Hu, Y. Li, W.A. Goddard, III, B. Zhang, H. Peng, E.H. Sargent, Stabilizing highly active Ru sites by suppressing lattice oxygen participation in

acidic water oxidation, J. Am. Chem. Soc. 143 (2021) 6482–6490, https://doi.org/10.1021/jacs.1c00384.

[12] Y. Yao, S. Hu, W. Chen, Z.-Q. Huang, W. Wei, T. Yao, R. Liu, K. Zang, X. Wang, G. Wu, W. Yuan, T. Yuan, B. Zhu, W. Liu, Z. Li, D. He, Z. Xue, Y. Wang, X. Zheng, J. Dong, C.-R. Chang, Y. Chen, X. Hong, J. Luo, S. Wei, W.-X. Li, P. Strasser, Y. Wu, Y. Li, Engineering the electronic structure of single atom Ru sites via compressive strain boosts acidic water oxidation electrocatalysis, Nat. Catal. 2 (2019) 304–313, https://doi.org/10.1038/s41929-019-0246-2.

[13] H. Jin, S. Choi, G.J. Bang, T. Kwon, H.S. Kim, S.J. Lee, Y. Hong, D.W. Lee, H. S. Park, H. Baik, Y. Jung, S.J. Yoo, K. Lee, Safeguarding the RuO2 phase against lattice oxygen oxidation during acidic water electrooxidation, Energy Environ. Sci. 15 (2022) 1119–1130, https://doi.org/10.1039/d1ee02636d.

[14] Y. Lin, Z. Tian, L. Zhang, J. Ma, Z. Jiang, B.J. Deibert, R. Ge, L. Chen, Chromium-ruthenium oxide solid solution electrocatalyst for highly efficient oxygen evolution reaction in acidic media, Nat. Commun. 10 (2019), 162, https://doi.org/10.1038/s41467-018-08144-3.

[15] J. Su, R. Ge, K. Jiang, Y. Dong, F. Hao, Z. Tian, G. Chen, L. Chen, Assembling ultrasmall copper-doped ruthenium oxide nanocrystals into hollow porous polyhedra: highly robust electrocatalysts for oxygen evolution in acidic media, Adv. Mater. (2018), 1801351, https://doi.org/10.1002/adma.201801351.

[16] S. Hao, M. Liu, J. Pan, X. Liu, X. Tan, N. Xu, Y. He, L. Lei, X. Zhang, Dopants fixation of Ruthenium for boosting acidic oxygen evolution stability and activity, Nat. Commun. 11 (2020), 5368, https://doi.org/10.1038/s41467-020-19212-y.

[17] N. Wang, S. Ning, X. Yu, D. Chen, Z. Li, J. Xu, H. Meng, D. Zhao, L. Li, Q. Liu, B. Lu, S. Chen, Graphene composites with Ru-RuO2 heterostructures: Highly efficient Mott–Schottky-type electrocatalysts for pH-universal water splitting and flexible zinc–air batteries, Appl. Catal. B. 302 (2022), 120838, https://doi.org/10.1016/j.apcatb.2021.120838.

[18] J. Wang, Y. Ji, R. Yin, Y. Li, Q. Shao, X. Huang, Transition metal-doped ultrathin RuO2 networked nanowires for efficient overall water splitting across a broad pH range, J. Mater. Chem. A. 7 (2019) 6411–6416, https://doi.org/10.1039/c9ta00598f.

[19] Z.L. Zhao, Q. Wang, X. Huang, Q. Feng, S. Gu, Z. Zhang, H. Xu, L. Zeng, M. Gu, H. Li, Boosting the oxygen evolution reaction using defect-rich ultra-thin ruthenium oxide nanosheets in acidic media, Energy Environ. Sci. 13 (2020) 5143–5151, https://doi.org/10.1039/d0ee01960g.

[20] K. Wang, Y. Wang, B. Yang, Z. Li, X. Qin, Q. Zhang, L. Lei, M. Qiu, G. Wu, Y. Hou, Highly active ruthenium sites stabilized by modulating electron-feeding for sustainable acidic oxygen-evolution electrocatalysis, Energy Environ. Sci. 15 (2022) 2356–2365, https://doi.org/10.1039/d1ee03610f.

[21] X. Cui, P. Ren, C. Ma, J. Zhao, R. Chen, S. Chen, N.P. Rajan, H. Li, L. Yu, Z. Tian, D. Deng, Robust interface Ru centers for high-performance acidic oxygen evolution, Adv. Mater. 32 (2020), 1908126, https://doi.org/10.1002/adma.201908126.

[22] K. Du, L. Zhang, J. Shan, J. Guo, J. Mao, C.C. Yang, C.H. Wang, Z. Hu, T. Ling, Interface engineering breaks both stability and activity limits of RuO(2) for sustainable water oxidation, Nat. Commun. 13 (2022), 5448, https://doi.org/10.1038/s41467-022-33150-x.

[23] B. Zhao, J. Liu, C. Xu, R. Feng, P. Sui, J.-X. Luo, L. Wang, J. Zhang, J.-L. Luo, X.-Z. Fu, Interfacial engineering of Cu2Se/Co3Se4 multivalent hetero-nanocrystals for energy-efficient electrocatalytic co-generation of value-added chemicals and hydrogen, Appl. Catal. B. 285 (2021), 119800, https://doi.org/10.1016/j.apcatb.2020.119800.

[24] J. Liu, X. Yang, F. Si, B. Zhao, X. Xi, L. Wang, J. Zhang, X.-Z. Fu, J.-L. Luo, Interfacial component coupling effects towards precise heterostructure design for efficient electrocatalytic water splitting, Nano Energy 103 (2022), 107753, https://doi.org/10.1016/j.nanoen.2022.107753.

[25] K.W. Kim, S.M. Kim, S. Choi, J. Kim, I.S. Lee, Electroless Pt deposition on Mn3O4 nanoparticles via the galvanic replacement process: electrocatalytic nanocomposite with enhanced performance for oxygen reduction reaction, ACS Nano 6 (2012) 5122–5129, https://doi.org/10.1021/nn300762m.

[26] C. Chowde Gowda, A. Mathur, A. Parui, P. Kumbhakar, P. Pandey, S. Sharma, A. Chandra, A.K. Singh, A. Halder, C.S. Tiwary, Understanding the electrocatalysis OER and ORR activity of ultrathin spinel Mn3O4, J. Ind. Eng. Chem. 113 (2022) 153–160, https://doi.org/10.1016/j.jiec.2022.05.024.

[27] L. An, F. Yang, C. Fu, X. Cai, S. Shen, G. Xia, J. Li, Y. Du, L. Luo, J. Zhang, A functionally stable RuMn electrocatalyst for oxygen evolution reaction in acid, Adv. Funct. Mater. 32 (2022), 2200131, https://doi.org/10.1002/adfm.202200131.

[28] F.J. Kresse G, Efficient iterative schemes for ab initio total-energy calculations using a plane-wave basis set, Phys. Rev. B. 54 (1996) 11169–11186, https://doi.org/10.1103/PhysRevB.54.11169.

[29] F.J. Kresse G, Efficiency of ab-initio total energy calculations for metals and_ semiconductors using a plane-wave basis set, Comp. Mater. Sci. 6 (1996) 15–50, https://doi.org/10.1016/0927-0256(96)00008-0.

[30] B.K. Perdew JP, Ernzerhof M., Generalized Gradient Approximation Made Simple, Perdew JP, Burke K, Ernzerhof M. 78 (1997), 1396, https://doi.org/10.1103/PhysRevLett.77.3865.

[31] P.E. Blochl, Projector augmented-wave method, Phys. Rev. B Condens Matter 50 (1994) 17953–17979, https://doi.org/10.1103/PhysRevB.50.17953.

[32] S. Grimme, J. Antony, S. Ehrlich, H. Krieg, A consistent and accurate ab initio parametrization of density functional dispersion correction (DFT-D) for the 94 elements H-Pu, J. Chem. Phys. 132 (2010), 154104, https://doi.org/10.1063/1.3382344.

[33] Y. Li, S.H. Chan, Q. Sun, Heterogeneous catalytic conversion of CO2: a comprehensive theoretical review, Nanoscale 7 (2015) 8663–8683, https://doi.org/10.1039/C5NR00092K.

[34] S. Chen, H. Huang, P. Jiang, K. Yang, J. Diao, S. Gong, S. Liu, M. Huang, H. Wang, Q. Chen, Mn-Doped RuO2 nanocrystals as highly active electrocatalysts for enhanced oxygen evolution in acidic media, ACS Catal. 10 (2019) 1152–1160, https://doi.org/10.1021/acscatal.9b04922.

[35] V. Selvanathan, M. Shahinuzzaman, S. Selvanathan, D.K. Sarkar, N. Algethami, H. I. Alkhammash, F.H. Anuar, Z. Zainuddin, M. Aminuzzaman, H. Abdullah, M. Akhtaruzzaman, Phytochemical-assisted green synthesis of nickel oxide nanoparticles for application as electrocatalysts in oxygen evolution reaction, Catalysts 11 (2021) 1523, https://doi.org/10.3390/catal11121523.

[36] A. Ramírez, P. Hillebrand, D. Stellmach, M.M. May, P. Bogdanoff, S. Fiechter, Evaluation of MnOx, Mn2O3, and Mn3O4 electrodeposited films for the oxygen evolution reaction of water, J. Phys. Chem. C. 118 (2014) 14073–14081, https://doi.org/10.1021/jp500939d.

[37] A. Ganguly, O. Anjaneyulu, A.K. Ganguli, Oxide-based nanostructures for photocatalytic and electrocatalytic applications, CrystEngComm 17 (2015) 8978–9001, https://doi.org/10.1039/C5CE01343G.

[38] F. Ji, Y. Men, J. Wang, Y. Sun, Z. Wang, B. Zhao, X. Tao, G. Xu, Promoting diesel soot combustion efficiency by tailoring the shapes and crystal facets of nanoscale Mn3O4, Appl. Catal. B. 242 (2019) 227–237, https://doi.org/10.1016/j.apcatb.2018.09.092.

[39] L. Xu, L. Yang, A. Liu, Facile one-pot synthesis of Mn3O4 nanorods and their analytical application, N. J. Chem. 45 (2021) 17576–17583, https://doi.org/10.1039/D1NJ02513A.

[40] L. Ai, Y. Wang, Y. Luo, Y. Tian, S. Yang, M. Chen, J. Jiang, Robust interfacial Ru-RuO2 heterostructures for highly efficient and ultrastable oxygen evolution reaction and overall water splitting in acidic media, J. Alloy. Compd. 902 (2022), 163787, https://doi.org/10.1016/j.jallcom.2022.163787.

[41] Q. Feng, Q. Wang, Z. Zhang, Y. Xiong, H. Li, Y. Yao, X.-Z. Yuan, M.C. Williams, M. Gu, H. Chen, H. Li, H. Wang, Highly active and stable ruthenate pyrochlore for enhanced oxygen evolution reaction in acidic medium electrolysis, Appl. Catal. B. 244 (2019) 494–501, https://doi.org/10.1016/j.apcatb.2018.11.071.

[42] C. Huang, X. Miao, C. Pi, B. Gao, X. Zhang, P. Qin, K. Huo, X. Peng, P.K. Chu, Mo2C/VC heterojunction embedded in graphitic carbon network: An advanced electrocatalyst for hydrogen evolution, Nano Energy 60 (2019) 520–526, https://doi.org/10.1016/j.nanoen.2019.03.088.

[43] K. Wu, C. Wang, X. Lang, J. Cheng, H. Wu, C. Lyu, W.-M. Lau, Z. Liang, X. Zhu, J. Zheng, Insight into selenium vacancies enhanced CoSe2/MoSe2 heterojunction nanosheets for hydrazine-assisted electrocatalytic water splitting, J. Colloid Interface Sci. 654 (2024) 1040–1053, https://doi.org/10.1016/j.jcis.2023.10.106.

[44] Y. Liu, J. Nan, L. Li, Y. Wang, Q. Shao, X. Zhu, Z. Lin, J. Ren, H. Algadi, R. Ge, Ruthenium oxide/cobalt oxide heterojunction electrocatalyst for biomass-derivative oxidation and hydrogen evolution, Adv. Compos Hybrid. Mater. 6 (2023) 163, https://doi.org/10.1007/s42114-023-00743-z.

[45] J. Joo, Y. Park, J. Kim, T. Kwon, M. Jun, D. Ahn, H. Baik, J.H. Jang, J.Y. Kim, K. Lee, Mn-dopant differentiating the Ru and Ir oxidation states in catalytic oxides toward durable oxygen evolution reaction in acidic electrolyte, Small Methods 6 (2022), 2101236, https://doi.org/10.1002/smtd.202101236.

[46] C. Lin, J.-L. Li, X. Li, S. Yang, W. Luo, Y. Zhang, S.-H. Kim, D.-H. Kim, S.S. Shinde, Y.-F. Li, Z.-P. Liu, Z. Jiang, J.-H. Lee, In-situ reconstructed Ru atom array on α-MnO2 with enhanced performance for acidic water oxidation, Nat. Catal. 4 (2021) 1012–1023, https://doi.org/10.1038/s41929-021-00703-0.

[47] T. He, S. Chen, B. Ni, Y. Gong, Z. Wu, L. Song, L. Gu, W. Hu, X. Wang, Zirconium-porphyrin-based metal-organic framework hollow nanotubes for immobilization of noble-metal single atoms, Angew. Chem. Int. Ed. 57 (2018) 3493–3498, https://doi.org/10.1002/anie.201800817.

[48] B. Zhao, J. Liu, X. Wang, C. Xu, P. Sui, R. Feng, L. Wang, J. Zhang, J.-L. Luo, X.-Z. Fu, CO2-emission-free electrocatalytic CH3OH selective upgrading with high productivity at large current densities for energy saved hydrogen co-generation, Nano Energy 80 (2021), 105530, https://doi.org/10.1016/j.nanoen.2020.105530.

[49] H. Fei, J. Dong, M.J. Arellano-Jimenez, G. Ye, N. Dong Kim, E.L. Samuel, Z. Peng, Z. Zhu, F. Qin, J. Bao, M.J. Yacaman, P.M. Ajayan, D. Chen, J.M. Tour, Atomic cobalt on nitrogen-doped graphene for hydrogen generation, Nat. Commun. 6 (2015), 8668, https://doi.org/10.1038/ncomms9668.

[50] R. Huang, Y. Wen, H. Peng, B. Zhang, Improved kinetics of OER on Ru-Pb binary electrocatalyst by decoupling proton-electron transfer, Chin. J. Catal. 43 (2022) 130–138, https://doi.org/10.1016/S1872-2067(21)63856-1.

[51] B. Zhao, J.-W. Liu, Y.-R. Yin, D. Wu, J.-L. Luo, X.-Z. Fu, Carbon nanofibers@NiSe core/sheath nanostructures as efficient electrocatalysts for integrating highly selective methanol conversion and less-energy intensive hydrogen production, J. Mater. Chem. A. 7 (2019) 25878–25886, https://doi.org/10.1039/c9ta09782a.

[52] Y. Qi, Y. Zhang, L. Yang, Y. Zhao, Y. Zhu, H. Jiang, C. Li, Insights into the activity of nickel boride/nickel heterostructures for efficient methanol electrooxidation, Nat. Commun. 13 (2022), 4602, https://doi.org/10.1038/s41467-022-32443-5.

[53] L. Hu, X. Zeng, X. Wei, H. Wang, Y. Wu, W. Gu, L. Shi, C. Zhu, Interface engineering for enhancing electrocatalytic oxygen evolution of NiFe LDH/NiTe heterostructures, Appl. Catal. B. 273 (2020), 119014, https://doi.org/10.1016/j.apcatb.2020.119014.

[54] Y. Jiang, J. Liu, Y. Jiang, Y. Mao, W. Shen, M. Li, R. He, Adjustable heterointerface-vacancy enhancement effect in RuO2@Co3O4 electrocatalysts for efficient overall water splitting, Appl. Catal. B. 324 (2023) 122294, https://doi.org/10.1016/j.apcatb.2022.122294.

[55] M. Etzi Coller Pascuzzi, A. Goryachev, J.P. Hofmann, E.J.M. Hensen, Mn promotion of rutile TiO2-RuO2 anodes for water oxidation in acidic media, Appl. Catal. B. 261 (2020), 118225, https://doi.org/10.1016/j.apcatb.2019.118225.

[56] Y. Zhao, J. Hu, C.-L. Chiang, Y. Li, W. Yang, Z. Yang, W.-H. Hung, Y.-G. Lin, Z. Chen, B. Li, P. Gao, H. Li, Ruthenium oxychloride supported by manganese oxide for stable oxygen evolution in acidic media, J. Mater. Chem. A 10 (2022) 20964–20974, https://doi.org/10.1039/d2ta05335g.

[57] C.F.D.Linsey C. Seitz, Kazunori Nishio, Yasuyuki Hikita, A.D.Joseph Montoya, Charlotte Kirk, Aleksandra Vojvodic, J.K.N.Harold Y. Hwang, Thomas F. Jaramillo, A highly active and stable IrO$_x$SrIrO$_3$ catalyst for the oxygen evolution reaction (https://www.science.org/doi/), Science 353 (2016) 1011–1014, https://doi.org/10.1126/science.aaf5050.

[58] L. Li, G. Zhang, J. Xu, H. He, B. Wang, Z. Yang, S. Yang, Optimizing the electronic structure of ruthenium oxide by neodymium doping for enhanced acidic oxygen evolution catalysis, Adv. Funct. Mater. 33 (2023), 2213304, https://doi.org/10.1002/adfm.202213304.

[59] W. Sun, Y. Song, X.-Q. Gong, L.-m Cao, J. Yang, An efficiently tuned d-orbital occupation of IrO$_2$ by doping with Cu for enhancing the oxygen evolution reaction activity, Chem. Sci. 6 (2015) 4993–4999, https://doi.org/10.1039/C5SC01251A.

[60] L. Giordano, B. Han, M. Risch, W.T. Hong, R.R. Rao, K.A. Stoerzinger, Y. Shao-Horn, pH dependence of OER activity of oxides: Current and future perspectives, Catal. Today 262 (2016) 2–10, https://doi.org/10.1016/j.cattod.2015.10.006.

[61] J. Rossmeisl, Z.W. Qu, H. Zhu, G.J. Kroes, J.K. Nørskov, Electrolysis of water on oxide surfaces, J. Electroanal. Chem. 607 (2007) 83–89, https://doi.org/10.1016/j.jelechem.2006.11.008.

[62] H.B. Tao, Y. Xu, X. Huang, J. Chen, L. Pei, J. Zhang, J.G. Chen, B. Liu, A general method to probe oxygen evolution intermediates at operating conditions, Joule 3 (2019) 1498–1509, https://doi.org/10.1016/j.joule.2019.03.012.

[63] X. Wang, X. Wan, X. Qin, C. Chen, X. Qian, Y. Guo, Q. Xu, W.-B. Cai, H. Yang, K. Jiang, Electronic structure modulation of RuO$_2$ by TiO$_2$ enriched with oxygen vacancies to boost acidic O$_2$ evolution, ACS Catal. 12 (2022) 9437–9445, https://doi.org/10.1021/acscatal.2c01944.

[64] H. Jin, X. Liu, P. An, C. Tang, H. Yu, Q. Zhang, H.J. Peng, L. Gu, Y. Zheng, T. Song, K. Davey, U. Paik, J. Dong, S.Z. Qiao, Dynamic rhenium dopant boosts ruthenium oxide for durable oxygen evolution, Nat. Commun. 14 (2023) 354, https://doi.org/10.1038/s41467-019-12886-z.

[65] V. Stamenkovic, B.S. Mun, K.J.J. Mayrhofer, P.N. Ross, N.M. Markovic, J. Rossmeisl, J. Greeley, J.K. Nørskov, Changing the activity of electrocatalysts for oxygen reduction by tuning the surface electronic structure, Angew. Chem. Int. Ed. 118 (2006) 2963–2967, https://doi.org/10.1002/ange.200504386.

[66] S. Niu, X.-P. Kong, S. Li, Y. Zhang, J. Wu, W. Zhao, P. Xu, Low Ru loading RuO$_2$/(Co,Mn)$_3$O$_4$ nanocomposite with modulated electronic structure for efficient oxygen evolution reaction in acid, Appl. Catal. B. 297 (2021), 120442, https://doi.org/10.1016/j.apcatb.2021.120442.